

*Carleton Geology Department*

*Geology Comps Papers*

---

*Carleton College*

*Year 2004*

---

# Geomorphic evidence for Martian climate change

Lisa Kanner  
Carleton College,

This paper is posted at Digital Commons@Carleton College.  
<http://digitalcommons.carleton.edu/gcp/8>

# **Geomorphic Evidence for Martian Climate Change**

Lisa Kanner  
Senior Integrative Exercise  
March 10, 2002

Submitted in partial fulfillment of the requirements for a Bachelor of Arts degree from  
Carleton College, Northfield, Minnesota

# **Geomorphic Evidence for Martian Climate Change**

Lisa Kanner  
Senior Integrative Exercise  
March 10, 2004

Advisors:  
Visiting Instructor, Sara Mitchell, Carleton College  
Drs. Carlton Allen and Mary Sue Bell, NASA-Johnson Space Center

## **Abstract**

Recent data from gamma-ray and neutron spectrometers on Mars Odyssey and high-resolution images from Mars Orbital Camera (MOC) on Mars Global Surveyor were used to determine whether high concentrations of polygonal terrain exist in areas of modern, stable water-ice. Small-scale polygonal terrain on Mars, as seen in meter-scale detail by MOC, is assumed to form from thermal contraction processes in ice-rich soil analogous to similar terrain on Earth. Previous studies have shown that the locations of polygonal terrain at high latitudes exist in areas with high concentrations of near-surface water-ice, thus suggesting that the terrain formed in equilibrium with modern climate conditions. This study expands comparison of polygon location and spectroscopy data using all available MOC images at mid-northern latitudes, 30°N to 65°N. Results show that high concentrations of polygonal terrain at mid-latitudes exist in areas of limited near-surface ice and where water-ice is not currently stable. Additional comparisons show that polygonal terrain exists across more than six geologic units of diverse age and origin and at a 5 km range of elevations. In addition, high albedo polygons, indicative of water-ice, are constrained to 55°N to 65°N, and low albedo polygons, indicative of significantly less ice, are confined to 40°N to 55°N. Finally, quantification of the preferential orientation of polygonal terrain reveals that the dominant orientation trends north-south and aligns parallel to topographic contours, analogous to terrestrial studies of polygonal networks. These results support the hypothesis that Martian polygons behave in a similar way to terrestrial polygons and that the presence of polygonal terrain at mid-northern latitudes suggests that their formation is representative of a previous Martian climate when Mars was at high (35°) obliquity and water-ice was stable at the surface at these latitudes.

**Keywords:** Mars, geomorphology, polygonal terrain, climate, ice

## Table of Contents

Introduction.....	1
Background.....	3
<i>Polygonal terrain on Earth and Mars.....</i>	<i>3</i>
<i>Geology of Mars.....</i>	<i>8</i>
<i>Ice and Martian climate history.....</i>	<i>10</i>
Methods.....	14
<i>Image analysis.....</i>	<i>15</i>
<i>Polygon fabric analysis.....</i>	<i>17</i>
Results.....	20
<i>Polygon and hydrogen distribution.....</i>	<i>20</i>
<i>Geology and elevation.....</i>	<i>29</i>
<i>Albedo and geometry of polygons.....</i>	<i>32</i>
<i>Preferred orientation and the auto-correlation function.....</i>	<i>32</i>
Discussion.....	36
Summary.....	43
Acknowledgements.....	45
References Cited.....	46
Appendix 1.....	50
Appendix 2.....	51
Appendix 3.....	55
Appendix 4.....	59

## Introduction

Recent results from the Mars Global Surveyor (MGS) and Mars Odyssey (MO) missions continue to expand current understanding of the global distribution of water and water-ice in the Martian regolith. Image datasets from Mars Orbital Camera (MOC) on MGS offer an exceptional new look at the red planet in unprecedented, meter-scale detail. One of the most striking geomorphic features clearly visible in the MOC images is a permafrost and periglacial feature known as polygonal terrain. Because Martian small-scale polygonal terrain is thought to be analogous to terrestrial ice-wedge polygons, which form in soils rich in water-ice, the presence of polygons on the surface can indicate the presence of water-ice in the subsurface at some point in geologic history. Results from gamma-ray and neutron spectrometers on MO show variations in the abundance of water-ice in the uppermost meter of the subsurface today. From the spectrometers, percentages of water-ice by mass for the uppermost meter of the entire planet can directly confirm distribution of water-ice today.

The combination of image and spectroscopy data can refine the location of subsurface ice to provide insight into Martian climate history. A positive correlation between spectroscopy data and distribution of ice-wedge polygons has been previously suggested for high latitudes on Mars (Mangold et al., 2003). In these high latitudes, there appear to be a higher density of polygonal terrain in regions of abundant water-ice in the near-surface (Mangold et al., 2003). This correlation indicates that current polygon distribution is in equilibrium with the current climate.

In this analysis, I expand the comparative study to mid-northern latitudes (Figure 1) on Mars with two goals: (1) to determine the relationships between the distribution and

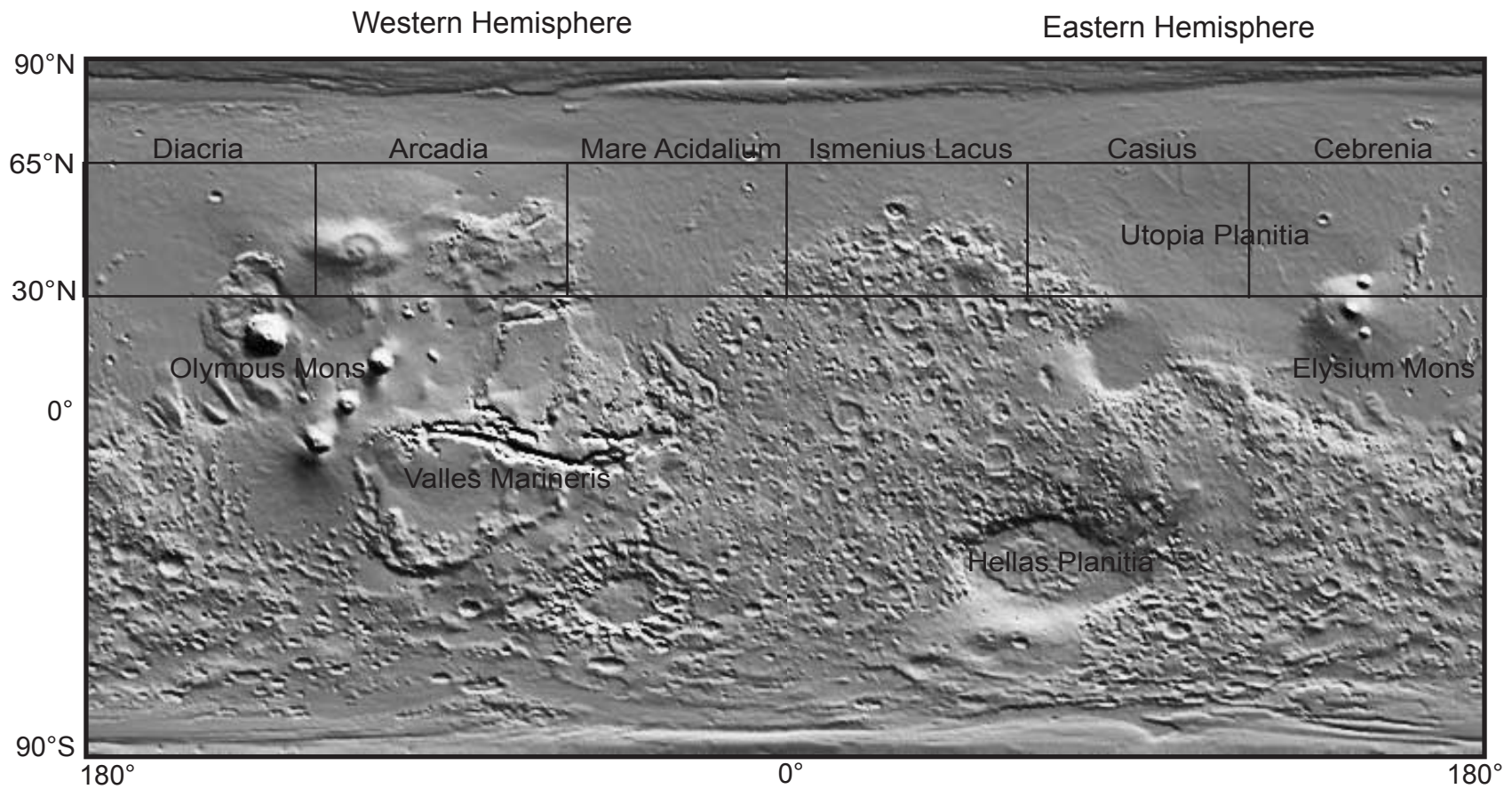


Figure 1. Shaded relief map of Mars. The study area is outlined and six quadrangles labeled. Map courtesy of <http://ltpwww.gsfc.nasa.gov/tharsis/shademap.html>.

appearance of polygonal terrain, hydrogen abundance, topography, and geology at these latitudes and (2) to use the relationships to re-evaluate assumptions that polygons exist in regions of current abundant near-surface ice and discuss the implications for Martian climate change. This systematic analysis of all available MOC images for the mid-northern latitudes is the most comprehensive and complete analysis done to date.

## **Background**

This study is founded on an analogy between ice-wedge polygons on Earth, which indicate the stability of water-ice in the subsurface, and small-scale polygons on Mars to examine the effects of variations in astronomical cycles on the stability and latitudinal distribution of water-ice in the Martian near-surface throughout geologic history.

### *Polygonal terrain on Earth and Mars*

The most recognizable terrestrial geomorphic indicators of subsurface ice include thermokarst pits, pingos, pseudocraters and patterned ground. Patterned ground features have geometric forms such as circles, polygons, stripes and nets. This study focuses on the polygonal form of patterned ground, selected because of its presence on the Martian surface and its recognition on Earth as an indication of subsurface ice.

Polygonal terrain is typically found in Arctic and Antarctic periglacial environments and is demarcated by troughs or cracks. Beneath each trough grows a vertical wedge composed, exclusively or partially, of ice and sand (Figure 2A). The general mechanism for formation of ice wedges is well known. When the thermal stress of the ground, induced by cooling winter temperatures, exceeds the tensile strength of the

(A) Terrestrial ice-wedge



(B) Terrestrial ice-wedge polygons



(C) Martian small-scale polygons

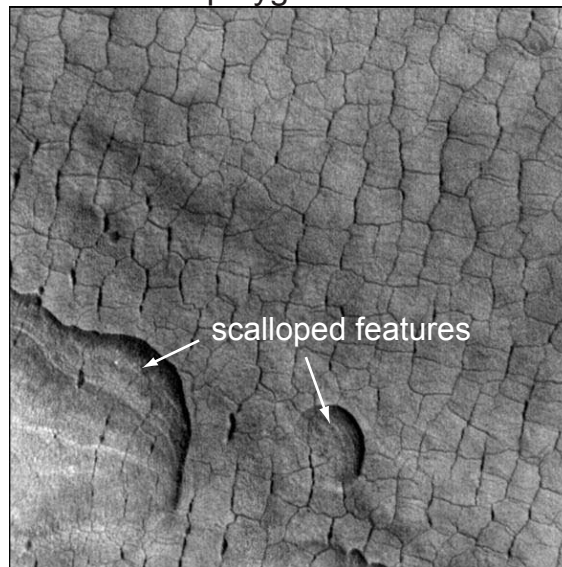


Figure 2. (A) Cross-section of a terrestrial ice-wedge. Ice-wedges can be up to 1 m across and 3 m deep. (B) An aerial photograph of a terrestrial polygon network. The size of individual polygons ranges from 5 to 30 m. Terrestrial polygons often align perpendicular or parallel to ancient shorelines and are frequently association with thermokarst pits, another permafrost feature. (C) Selection from MOC satellite image M040331 of Martian small-scale polygons. Average polygonal width of Martian polygons is 100 m. Scalloped features are thought to be analogous to terrestrial thermokarst pits. Both terrestrial images are from the Canadian Arctic.



ground, a crack will form (Lachenbruch, 1962). Warming spring temperatures cause the frozen water to melt and move down the thermal contraction crack where it will eventually freeze in winter. Should permafrost conditions persist, the wedge will be preserved below the depth of annual freeze-thaw and the contraction process will repeat itself the following winter (Lachenbruch, 1962). As a zone of weakness, the initial thermal contraction crack is often re-activated each cycle. That is, water melts and freezes in the same crack resulting in the growth of a single wedge (Lachenbruch, 1962; Mackay and Burn, 2002). Terrestrial wedges can be several meters deep and polygons tens to hundreds of meters across (Kerfoot, 1972; Lachenbruch, 1962; Pratt, 1958) (Figure 2B). The crack spacing of terrestrial polygons is typically 3 to 10 times the crack depth (Mellon, 1997).

Morphology of terrestrial polygons may provide indications of their relative age and environmental conditions at the time of their formation. The combination of field research and computer analysis shows that in early stages of polygonal growth, initial cracks are curvilinear and long, reaching up to 80 meters (Mackay and Burn, 2002). The next fractures to develop commonly intersect the initial crack at right angles, producing networks of irregular rectilinear patterns (Mackay and Burn, 2002; Plug and Werner, 2001; Sletten et al., 2003). Further polygonal development leads to formation of wedges at new angles  $>90^\circ$ , in combination with the secession wedge growth at other angles. Thus, five- and six-sided polygons with straight sides and intersection angles of  $120^\circ$  are typical of highly evolved polygonal systems (Plug and Werner, 2001; Sletten et al., 2003).

Some observations of terrestrial polygons have shown that the orientation of polygonal troughs can be a function of topography. Mackay (1995; 2002) observed that the predominant orientation of the primary (longest) cracks is normal to topographic contours while secondary cracks typically form parallel to the contours. Although it is more common for polygon orientation to be perpendicular to topography, polygons have been observed to align parallel to topography (Mackay, telephone communication). Opposing polygonal sides are also known to align either parallel or perpendicular to ancient shorelines and existing meltwater channels (Gray and Seppala, 1991; Mackay, 1995). In this way, a preferential orientation of polygon sides can indicate topographic variation or the presence of a body of water, past or present. Formation and morphologic implications of terrestrial polygons is applicable for further study of Martian polygons.

Polygonal terrain is the dominant form of patterned ground seen on Mars and has been identified on the Martian surface in older high-resolution Viking Orbiter images (Brook, 1982; Carr and Schaber, 1977; Evans and Rossbacher, 1980; Morris and Underwood, 1978), Viking Lander 2 images (Mutch et al., 1977), and now in more recent MOC images (Mangold, 2003; Mellon, 1997; Seibert and Kargel, 2001) (Figure 2C). Based on morphology and mechanism of formation, Martian polygonal ground subdivides into two categories, large-scale and small-scale polygons. Large-scale polygons, which are found only in the northern plains, are 3-10 km across with trough widths of 200-800 m (Helfenstein and Mouginis-Mark, 1980; Pechmann, 1980). Small-scale polygons range from 20-100 m across and exist in mid- and high-latitudes of both hemispheres (Mellon, 1997). The widths and depths of these troughs cannot be measured

with current orbital images. Thus, orders of magnitude separate large-scale and small-scale polygons and polygonal terrain of intermediate size has not been observed.

Another fundamental distinction between large-scale and small-scale polygons on Mars is the proposed respective origin of formation. Two mechanisms have been proposed for the formation of small-scale polygons: (1) desiccation of sediment analogous to terrestrial mud cracking (Seibert and Kargel, 2001) and (2) ice- or sand-wedging formed from thermal contraction processes, analogous to terrestrial periglacial ice-wedge polygons (Mellon, 1997; Seibert and Kargel, 2001). Because of the large scale,  $10^1$  to  $10^2$  m, it is unlikely that small-scale polygonal terrain is a result of mud-cracking. However, the similar geometry and strong association of small-scale polygonal terrain with other surface ice indicators suggests that Martian polygons are ice features resulting from thermal contraction cracking (Mellon, 1997; Seibert and Kargel, 2001). Small-scale polygonal terrain is the focus of this study based on the assumption that the presence of polygons on the surface is indicative of the presence of water-ice in the subsurface at some point in the past.

Several possible mechanisms of formation may explain large-scale polygons. The most pertinent theory to this study includes a mechanism described by Hiesinger and Head (2000). Analyzing the topographic distribution of large-scale polygons in mid-northern latitudes on Mars, they conclude that formation is tectonic caused by uplift resulting from the removal of the water and water-ice load in former standing bodies of water. They postulated such bodies of water in the Utopia Basin, a circular feature 3000 km in diameter, centered at about  $270^\circ$  longitude and  $45^\circ$  latitude (Hiesinger and Head, 2000). The existence of former lakes in the Utopia Basin may be relevant to this study.

Such a large body of water could provide a source of subsurface water-ice and also influence the formation and development of small-scale polygonal terrain. Because terrestrial ice-wedge polygons are known to preferentially form along meltwater channels and shorelines, it is possible that Martian small-scale polygons would preferentially develop in or along old lake basins, and thus low elevations, like the Utopia Basin. Further description of the geology of the Utopia Basin in the context of the entire study area is described in the following section.

### *Geology of Mars*

The major geologic division of Mars, known as the crustal dichotomy, separates the southern highlands from the northern lowlands. This highland-lowland boundary originates from either a period of huge impacts or tectonics (Tanaka et al., 1992). Further separation of geologic units is based on major periods of geologic activity divided into three chronostratigraphic epochs: the Noachian, Hesperian and Amazonian (Hartmann and Neukum, 2001) (Figure 3). The study area is bounded by the northern latitudes of 30° and 65° and is located, for the most part, in the northern lowlands. These plains, lying predominantly below the 0-km elevation datum, consist of Hesperian and Amazonian materials of predominantly volcanic and sedimentary origin (Tanaka et al., 1992).

Further understanding of Martian geology comes from studies of thermal inertia and gravity anomalies. Thermal inertia is defined by the amplitude of diurnal temperature variation of a body and expressed by the equation,  $I = (k\rho C)^{1/2}$ , in units of  $10^3 \text{ cal/cm}^2 \cdot \text{s}^{1/2} \cdot ^\circ\text{K}$ , where  $I$  is the thermal inertia,  $k$  is the thermal conductivity,  $\rho$  is the

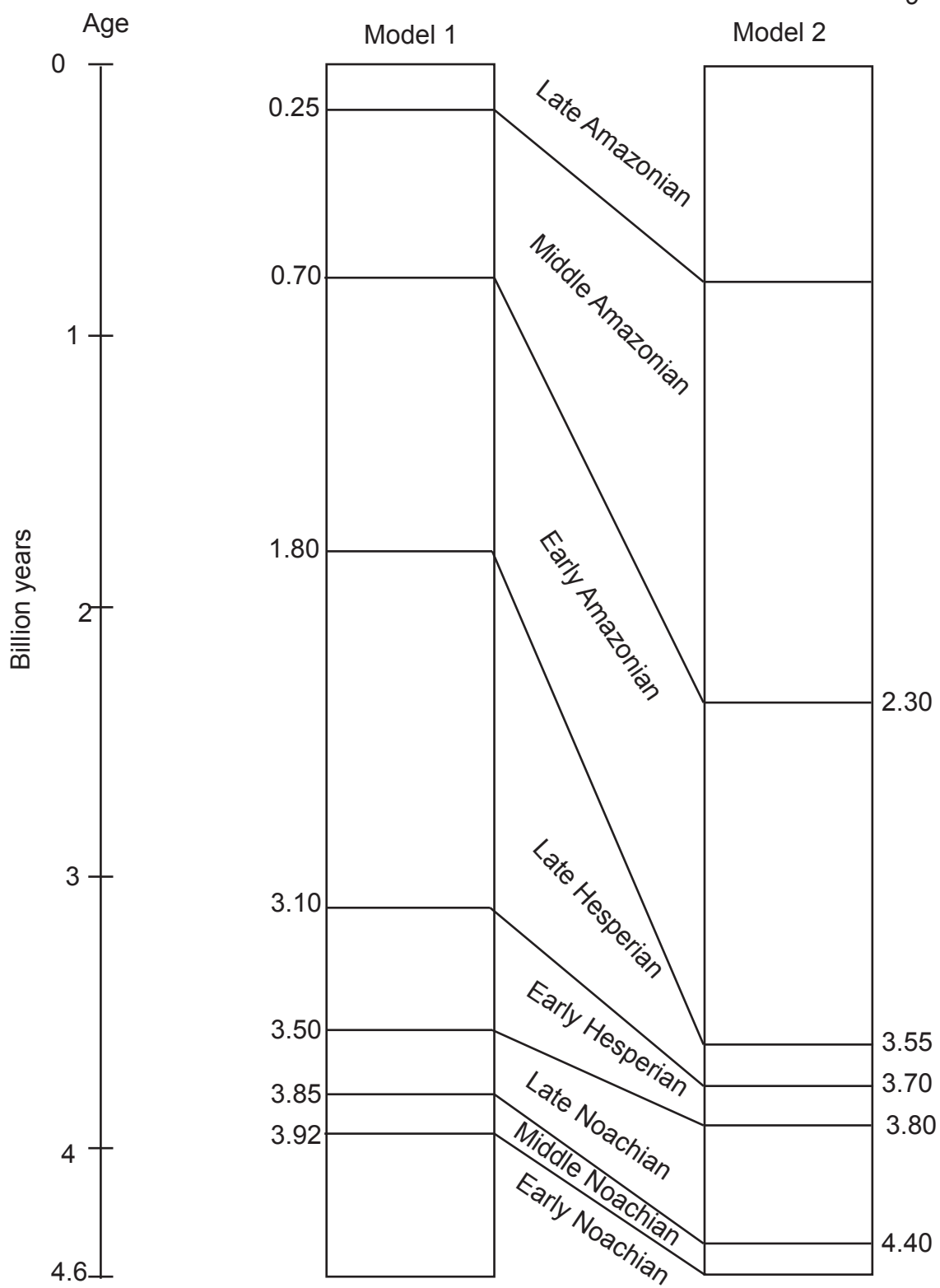


Figure 3. Martian geologic time scale based on crater fluxes, showing two chronologies. Model 1 is from Neukum and Wise (1976), Model 2 is from Hartmann et al., (1981).

bulk density, and  $C$  is the specific heat (Christensen and Moore, 1992). Laboratory experiments show that thermal inertia values correlate with particle size (Wechsler and Glaser, 1965). Small, loose sediments produce low thermal inertia values and solid rock produces high values (Christensen and Moore, 1992). Planet-wide thermal inertia values have been calculated on several Martian missions and range from 1 to  $15 \times 10^{-3} \text{ cal/cm}^2 \text{ s}^{1/2}$  K. For comparison, solid rock yields a thermal inertia value of  $\sim 60$  (Mellon and Jakosky, 1993). In the study area, thermal inertia values are highest in the region of Utopia Planitia.

Gravity variations have also been evaluated planet-wide and a gravity high is again associated with the Utopia Planitia region. This high corresponds to the topographic low, centered at about  $45^\circ\text{N}$ ,  $270^\circ\text{W}$ . The combination of these data provide strong indication that this depression represents a large ancient impact basin that, some suggest (Hiesinger and Head, 2000), may have been a repository for water under a previous Martian climate.

### *Ice and Martian Climate History*

Geomorphic evidence clearly shows that Mars has undergone climate change on both long and short time scales. Large-scale climate changes, with respect to the distribution of  $\text{CO}_2$  in the atmosphere, Martian surface temperature, and internal heat flow, are in part recorded in the morphology of valley networks (Fanale et al., 1992). Valley networks indicate the presence of liquid water early in the planet's history  $\sim 3.6$  Gya that was removed from the surface during the early Hesperian  $\sim 3.5$  Gya (Fanale et al., 1992). However, a significant reservoir of water may still exist in the subsurface in

the form of ground ice. The presence of geomorphic ice features, including rampart craters, debris flows, thermokarst pits, and patterned ground, provides evidence of ground ice at nearly all latitudes (Allen, 1979; Carr and Schaber, 1977; Mouginis-Mark, 1979). The current spatial distribution of these geomorphic ice features can be explained in part by small-scale climate changes resulting from dramatic variations in orbital parameters (Head et al., 2003; Kieffer and Zent, 1992).

Short-term climate fluctuations on Earth, as seen in the geologic records, are at least in part driven by the planet's astronomical cycles. These cycles are known as the Milankovich cycles and the parameters pertinent to this study include variations in obliquity, defined as the tilt of a planet's spin axis, and eccentricity, defined as the ellipticity of a planet's orbit. Similar orbital variations have been calculated for Mars and are significantly more dramatic than those on Earth (Kieffer and Zent, 1992) (Table 1). On Mars, these fluctuations are thought to have significant effects on the amount of insolation and thus the division of volatiles between the atmosphere and surface (Kieffer and Zent, 1992). For Mars, obliquity, rather than eccentricity, is considered the primary factor in controlling periodic climate change. A decrease in obliquity from its present average value would cause decreases in polar-cap temperature, atmospheric temperature, and in the amount of atmospheric dust, which combined result in the retreat of H<sub>2</sub>O poleward (Kieffer and Zent, 1992). An increase in obliquity from its minimum value would have the reverse effects in temperature and H<sub>2</sub>O distribution (Kieffer and Zent, 1992). Thus, in response to oscillations in obliquity, geomorphic evidence and modeling suggests that water-ice has been stable at different latitudes in past and present climates

(Allen, 1979; Carr and Schaber, 1977; Mellon and Jakosky, 1993; Mischna et al., 2003; Mouginis-Mark, 1979).

Table 1. Orbital Parameters

Planet	Obliquity (degrees)	Obliquity Periodicity (10 <sup>3</sup> yr)	Eccentricity <sup>a</sup>	Eccentricity Periodicity (10 <sup>3</sup> yr)
Earth	22-24.5	41	0.01-0.05	100 and 400
Mars	25.2 +/-10.3	125	0.00-0.13	175

<sup>a</sup> the ratio of the distance between the foci of the orbit to length of the major axis

The stability of ice on Mars is dependant on several parameters, including the amount of water vapor in the atmosphere, the size of the polar CO<sub>2</sub> caps, the average pore radius of the Martian regolith, the thermal and diffusive properties of the regolith, as well as the surface and subsurface temperatures (Mellon and Jakosky, 1993). Various models estimate trends in the latitudinal distribution and stability of ground ice throughout geologic history (Clifford and Hillel, 1983; Farmer and Doms, 1979; Paige, 1992). These models suggest that atmospheric water-ice will condense and be stable on the Martian surface in areas where the mean annual surface temperature is less than the frost point temperature, the temperature at which the mean atmospheric water vapor density will saturate (Mellon and Jakosky, 1993). On Mars, the frost point temperature is equal to 196 K. At the current obliquity of 25°, surface ice is stable poleward of ~50°, and at high obliquities of 40°, surface ice is stable poleward of ~30° (Mellon and Jakosky, 1993) (Figure 4).

Under the present climate regime, recent results from the gamma-ray and neutron spectrometers on Mars Odyssey provide direct results for the abundance of water-ice today. Data from these spectrometers indicate the presence of a hydrogen-rich layer tens of centimeters thick in the uppermost meter in high latitudes, > 60° (Boynton et al., 2002;



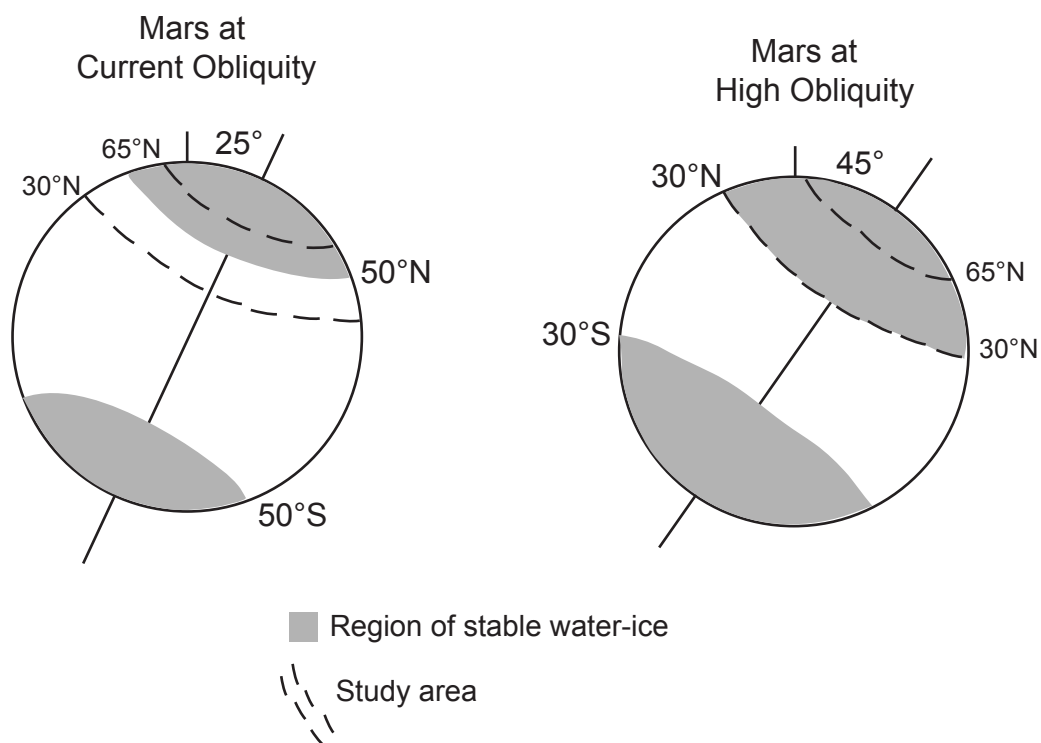


Figure 4. Predicted regions of ice stability at current obliquity and at high obliquity (Mellon and Jakosky, 1997; Mischna, 2003). The stability of water-ice moves equatorward with increasing obliquity. For the past ~300 kyr Mars's obliquity has remained at ~25° (Head et al., 2003). However, between 400 and 2,100 kyr estimated obliquity reached and often exceeded 30° (Head et al., 2003).

Feldman et al., 2002; Mitrofanov et al., 2002). Because of its correlation to models of ice stability, this hydrogen-rich layer is inferred to indicate regions of present water-ice stability (Boynton et al., 2002; Feldman et al., 2002; Mellon and Jakosky, 1993). Data suggest that water-ice constitutes 35+/- 15% by weight of the shallow subsurface near the north and south polar regions (Boynton et al., 2002). The idea that modern ice distribution may not correlate directly with geomorphic ice indicators because of short-term climate fluctuations is tested in this study by combining these spectroscopy data with MOC images showing the location of polygonal terrain.

## **Methods**

The methods described below aim to constrain the locations of subsurface ice on Mars by determining relationships between the distribution and appearance of polygonal terrain and the distribution of water-ice, geology and topography. Because previous studies, e.g. Seibert and Kargel, 2001, have shown a concentration of polygonal terrain in the Casius Quadrangle, bounded by 240°W to 300°W and 30°N to 65°N, more detailed methods were used for this region. The use of all available MOC images achieves a comprehensive systematic analysis of Martian polygonal terrain in mid-northern latitudes. Comparison of the location of polygonal terrain to spectroscopy data between 30°N and 65°N tests the hypothesis that modern ice distribution may not correlate to locations of water-ice related geomorphologic features. Examination of the material that constitutes polygon troughs also suggests variation in present and past water-ice distribution. Further comparison of MOC images showing the presence of polygonal terrain to geologic and topographic data indicates whether Martian polygons develop

analogous to terrestrial polygons. Quantification of the geometry of polygonal networks provides further insight into Martian polygon development.

### *Image Analysis*

Using 5,782 high-resolution, narrow-angle MOC images (1.55-12.39 m/pixel), polygonal terrain was mapped in a latitude band from 30°N to 65°N (Malin et al., 2003-2004). Datasets from August 1997 to February 2003 were used with the exclusion of the September 1999 to February 2000 set. This set was eliminated because the images were obtained during a northern winter and the presence of frost inhibited basic examination. Individual images cover an area of 1.5 km to 3 km (512-1072 pixels) in width and 9 km to 173 km (1792 – 198240 pixels) in length. The presence, absence, or possibility of polygonal terrain was cataloged with the corresponding image number, latitude, longitude, and further description of geomorphology. The ratio of the number of MOC images showing the presence of polygonal terrain with respect to the total number of MOC images showing the presence, absence, or possibility was determined for five-degree latitudinal bands between 30°N and 65°N.

The gamma-ray spectrometer, neutron spectrometer, and high-energy neutron detector on MO have surveyed the planet for hydrogen in the uppermost meter. Measurements of the global distributions of epithermal neutron flux energies captured by the neutron spectrometer are of particular importance. Because epithermal neutron flux rates are inversely related to water-ice abundance in the uppermost meter, it is possible to map the distribution of ice in the near subsurface (Boynton et al., 2002; Feldman et al., 2002). The corrected epithermal neutron flux rate data in 2 x 2 degree cells was mapped

to show the relative distribution of hydrogen between 30°N and 65°N and flux rate data in 0.5 x 0.5 degree cells was used for the Casius Quadrangle (Boynton, e-mail communication). The average flux rate was calculated for five-degree latitudinal intervals for the entire study area as well as the Casius Quadrangle. Near-surface ice abundance was then compared with the locations of polygonal terrain in the MOC images to establish whether regions of high near-surface ice match regions with high concentrations of polygonal terrain. For the Casius Quadrangle, the actual number of MOC images revealing polygonal terrain was determined for areas with flux rates greater than and less than the average value for the entire quadrangle.

The distribution of MOC images showing the presence of polygonal terrain was also compared to maps of geology, modified from (Greeley and Guest, 1987), topography (Milliken, e-mail communication) and thermal inertia (Putzig et al., 2003). Observations were made to determine the number of MOC images to each geologic unit in the study area. Meter-scale elevation was determined for the location, rounded to the nearest whole degree latitude and longitude, for each MOC image. The elevations were categorized for the range of elevation values between 30°N and 65°N at 500 m intervals. Because comprehensive data was not available for comparison to thermal inertia values, general associations were made between concentrations of polygonal terrain and grain size derived from these values.

Systematic analysis of all MOC images showing the presence of polygonal terrain was conducted to categorize the images based on the albedo of the polygonal troughs. Because the albedo of a body is a function of the reflectivity of the material, high albedo and low albedo material may indicate the presence or absence of near-surface ice. Since

water-ice is more reflective than bedrock or soil, polygonal troughs containing a high albedo material likely suggest the presence of near-surface ice. Troughs with low albedo material may imply the absence of near-surface ice. Images showing these features were labeled “icy polygons” and “sublimation polygons”, respectively (Figure 5). Images were labeled “intermediate albedo” when the appearance of the polygons seemed to represent neither ice nor sublimation.

### *Polygon fabric analysis*

Because the preferred orientation of polygonal terrain may correlate to topographic variations and ancient shorelines, an image analysis technique known as the autocorrelation function (ACF) was used to quantify the preferential orientation of polygons. The autocorrelation function has been used in terrestrial studies to quantify the shape and preferred orientations of minerals in plastically deformed rocks using photomicrographs (Davidson et al., 1996; Panozzo, 1992). To use the ACF for analysis of Martian polygons, which are eight orders of magnitude greater in size than individual mineral grains, is appropriate because the ACF is unitless, and is only dependant on the brightness of the original image at all x- and y-coordinates (Panozzo, 1992). Because polygonal troughs have a higher or lower albedo compared to the background of the Martian regolith, the ACF can be used to quantify directions of preferred orientation exhibited by the troughs. Further description of the ACF is given in Appendix 1. A total of 22 MOC images were used for ACF analysis (Figure 6). Images were selected where polygonal terrain covered at least 75% of the image, appeared to be unaffected by other geomorphologic features, and existed in an evenly illuminated area. Reported angles of

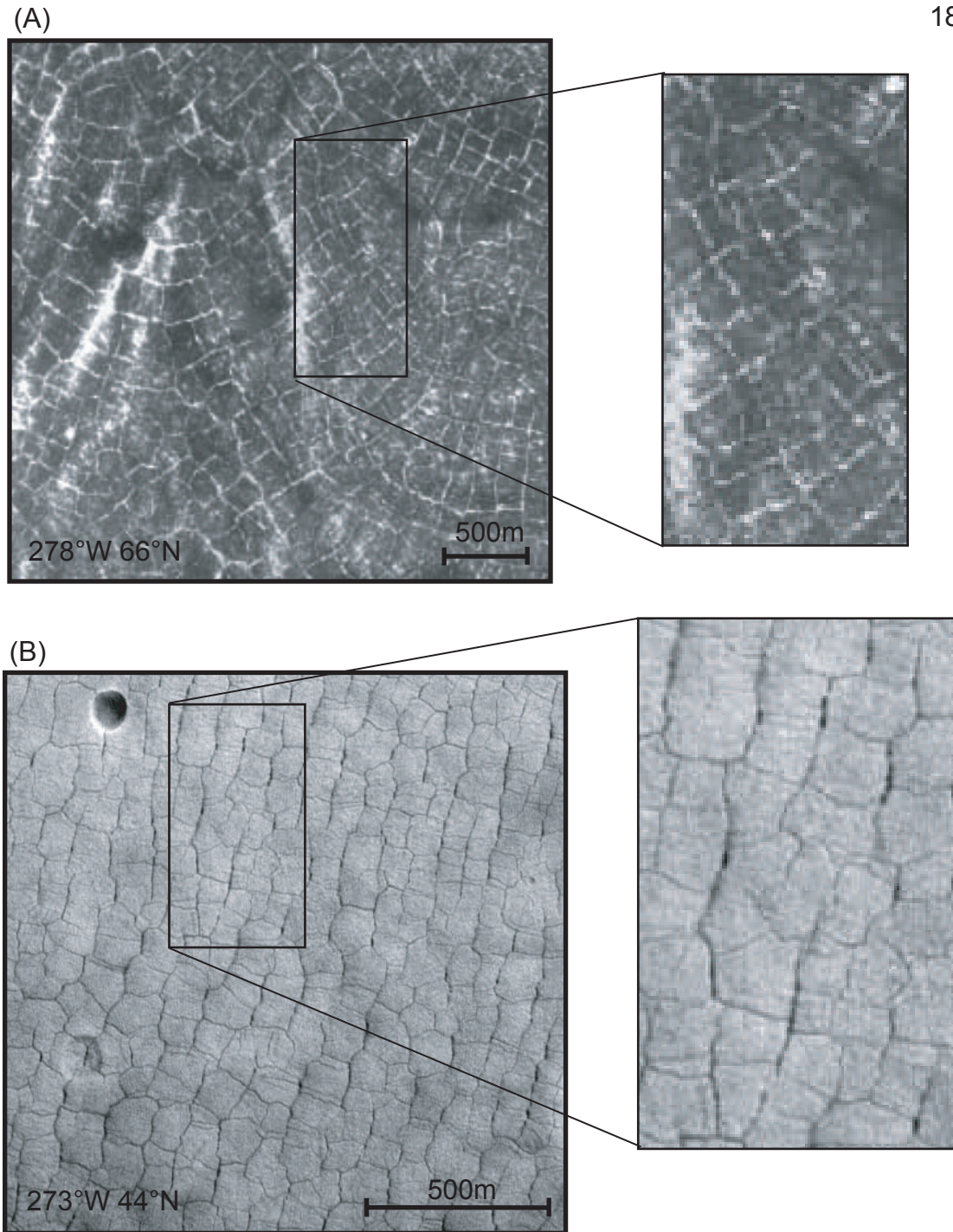


Figure 5. Comparison of polygonal terrain at high-latitudes, 66°N, and mid-latitudes, 44°N. (A) Selection from MOC image M190234 and (B) selection from MOC image M0304331. The bright material present in (A), the high-latitude polygons may indicate the presence of near-surface ice. The dark colored troughs in (B), the low-latitude polygons, may represent sublimation of near-surface ice.

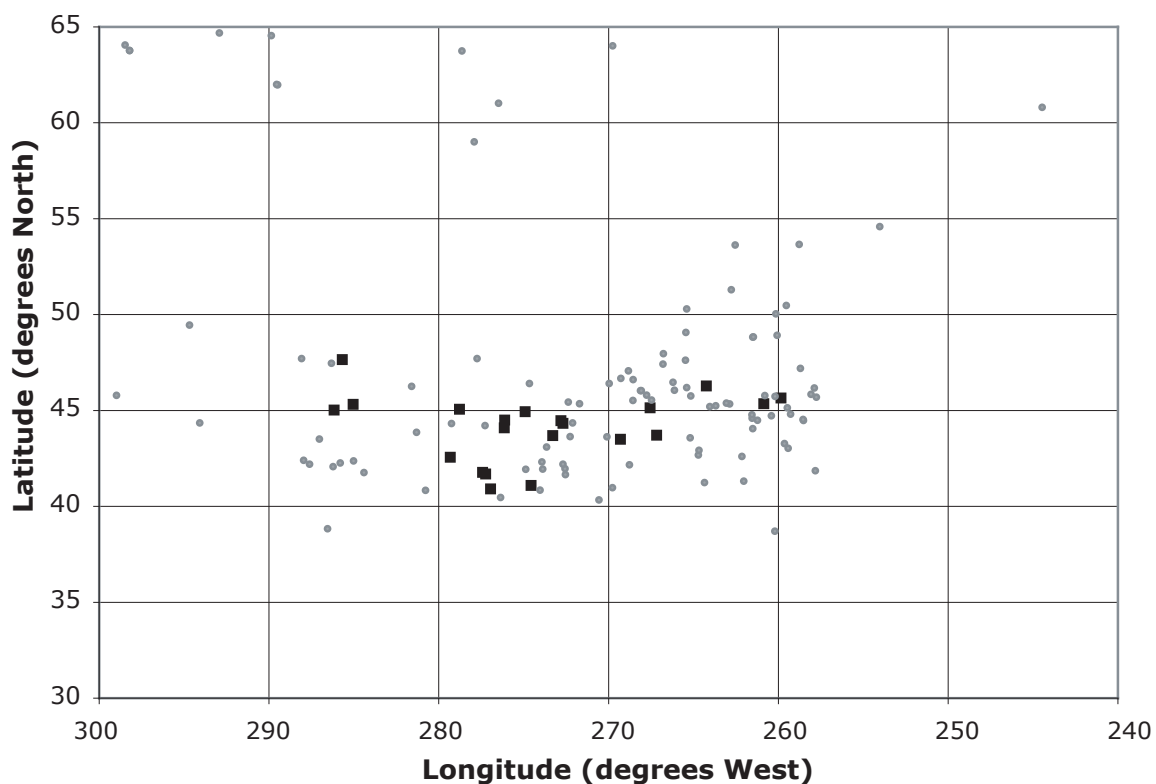


Figure 6. The 22 locations of MOC images (black squares) used for ACF analysis. Images were selected from the total number of MOC images that reveal polygonal terrain in the Casius Quadrangle. The MOC image number, latitude, and longitude are recorded in Appendix 4, Table 3A.

preferred orientation were determined measuring the strike of the major axis of the ellipse in the ACF (Appendix 1).

Because the orientation of the polygonal terrain may be a function of topography, specific elevation analysis was conducted for ACF images and the area that includes the locations of ACF images. Meter-scale elevations were determined for each MOC image used in ACF analysis and variations in elevation were analyzed at 100 m intervals for the elevation range of all the ACF images. Elevation data in 2 x 2 degree cells were collected and expressed as a topographic map for the area that includes the locations of all ACF images. For similar latitude and longitude coordinates, the topographic map of the selected area was compared to the plot of the orientations of the ACF images to determine whether the orientation of polygons aligns parallel, perpendicular, or at divergent angles to the topographic contour.

## **Results**

### *Polygon and hydrogen distribution*

The distribution of MOC images analyzed between 30°N-65°N is shown in Figures 7 and 8. Of the total images analyzed, including those that contained error in the image processing, 4.2 % revealed the presence of polygonal terrain (Appendix 2, Table A1) (Figure 9). Few polygons were identified south of 35°N or in the cratered highlands. The latitudinal comparison of the percentage of MOC images revealing the presence of polygonal terrain to images that reveal the presence, absence, and possibility of polygonal terrain is greater than 6.0% in latitude intervals of 40°N-45°N, 45°N-50°N, and 60°N-65°N and less than 6.0% in the remaining latitude intervals (Figure 10). A particularly



## Western Hemisphere

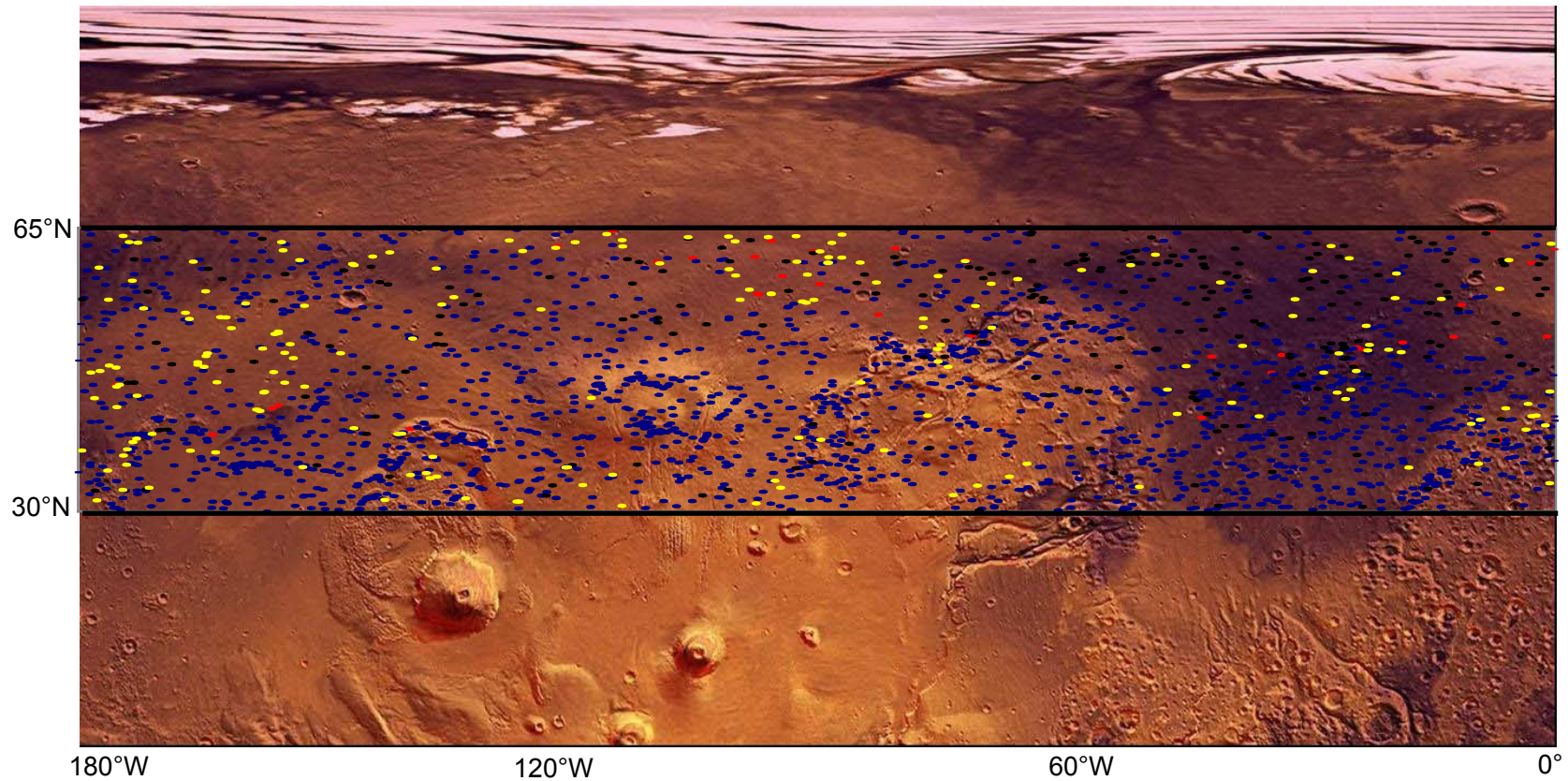


Figure 7. Distribution of all Mars Orbital Camera (MOC) images analyzed in the north western hemisphere of Mars indicating the presence of polygonal terrain (red), absence (blue), possibility (yellow), and images with error processing (black). The number of MOC images analyzed for the entire study area is 5,782.

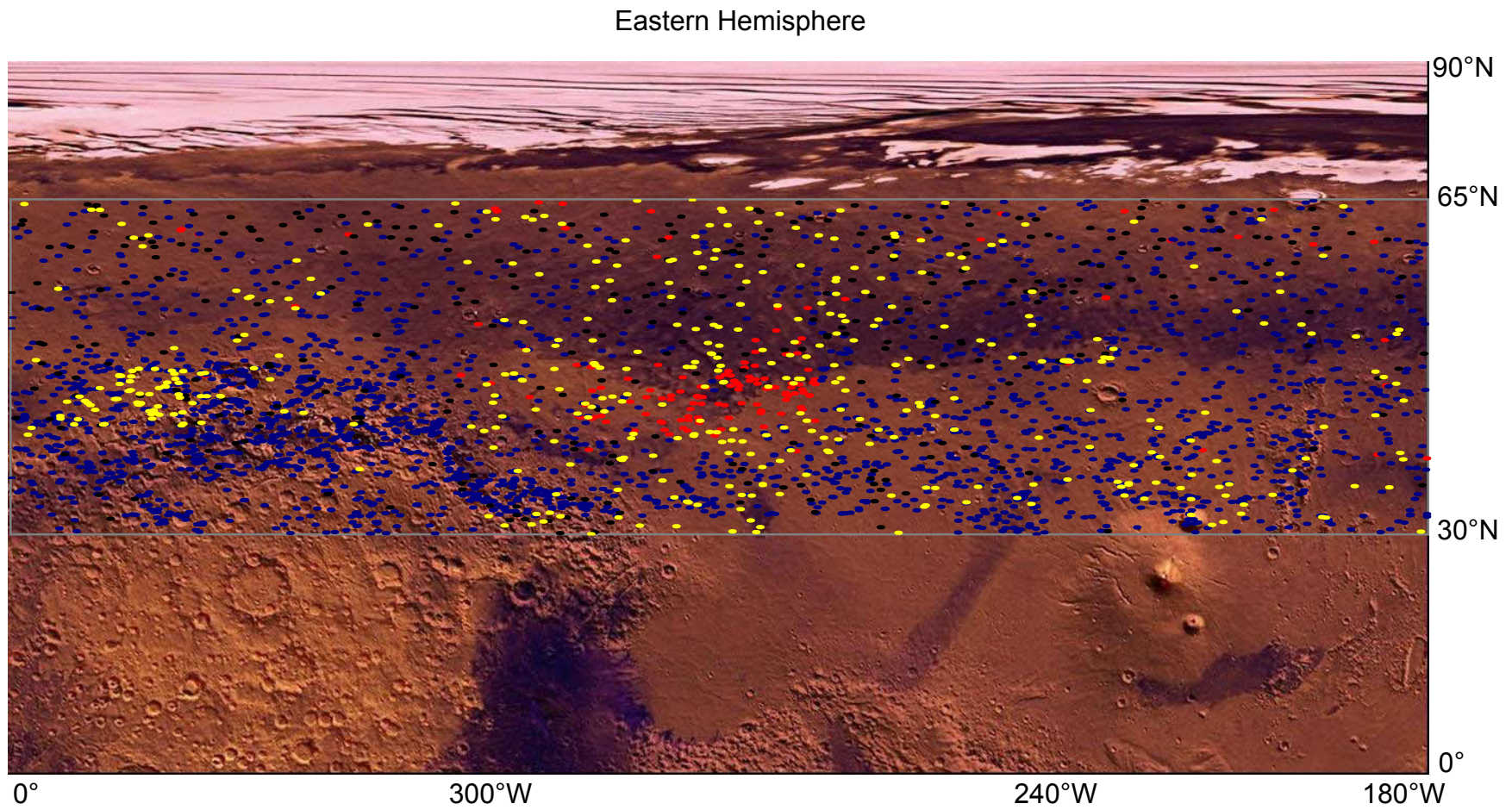


Figure 8. Distribution of all MOC images analyzed in the north eastern hemisphere of Mars indicating the presence of polygonal terrain (red), absence (blue), possibility (yellow), and images with error processing (black).



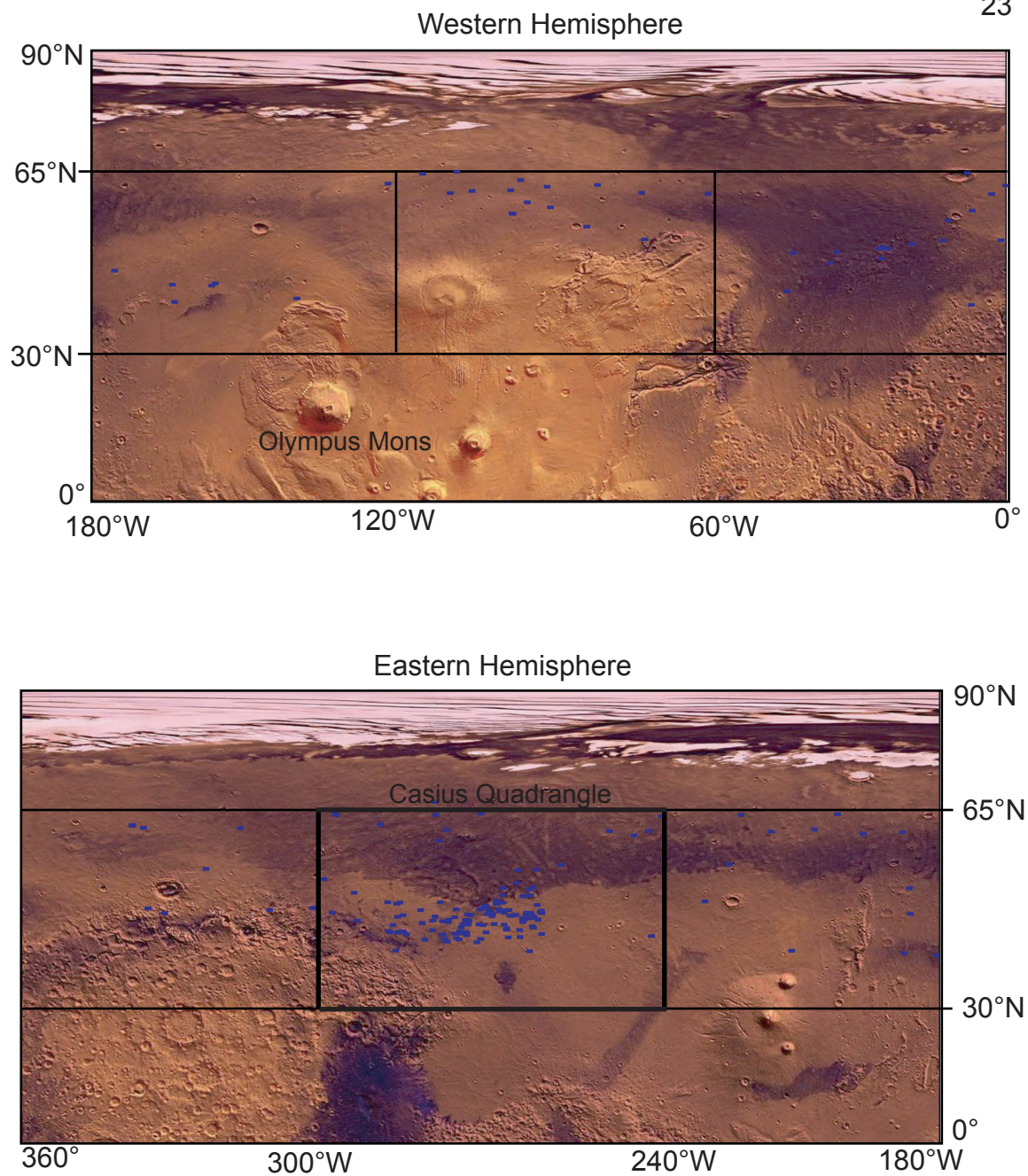


Figure 9. Distribution of MOC images revealing the presence of polygonal terrain. Of the total images analyzed, 4.2% reveal the presence polygonal terrain. The concentration of polygonal terrain is highlighted by the Casius Quadrangle.

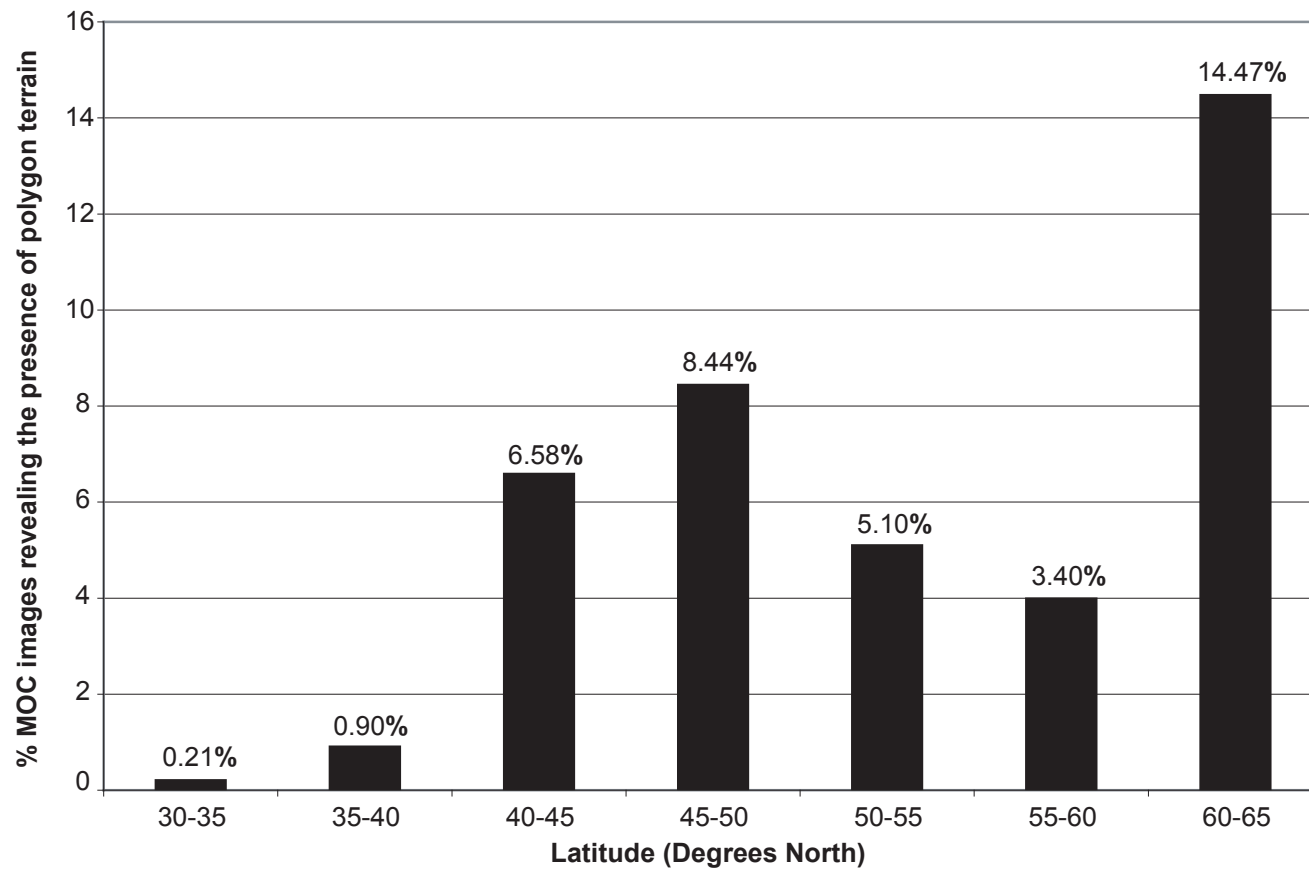


Figure 10. Latitudinal distribution of MOC images revealing the presence of polygonal terrain. Percentages are calculated based on the number of MOC images showing polygonal terrain and the total number of MOC images showing the presence, absence, and possibility of polygonal terrain.

high concentration of polygonal ground is present in the Casius Quadrangle between 288°W-258°W and 40°N-50°N (Figure 11). In this region of western Utopia Planitia, 52% of the total 191 images analyzed show the presence of polygonal terrain.

Average concentrations of hydrogen calculated at five-degree latitudinal intervals increase poleward. For the entire study area, epithermal flux rate data, which is inversely related to hydrogen abundance, in 2 x 2 degree cells decreases from an average value of 7.727 at 30°N-35°N to 4.465 at 60°N-65°N. The rate of decrease is -0.54 epithermal counts per five degrees latitude and is determined from a best-fit line of five-degree latitudinal intervals between 30°N-65°N plotted against average epithermal counts (Figure 12). For the Casius Quadrangle, flux rate data graphed from 0.5 x 0.5 degree cells, reaches its highest, and thus hydrogen reaches its lowest, abundance between 40°N-45°N and flux rate data reaches its lowest, and thus hydrogen its highest, abundance value between 60°N-65°N (Figure 12).

Because the average value for the entire Casius Quadrangle is 7.806, a value of 8.0 was used as a transition point to determine number of MOC images showing the presence polygonal terrain in areas of high-hydrogen content ( $< 8.0$ ) and low hydrogen content ( $> 8.0$ ). Of the 127 MOC images in the entire quadrangle that reveal the presence of polygonal terrain 114, or 90%, are located in regions of low-hydrogen content. Only 13 MOC images, or 10%, are located in regions of high-hydrogen content. The highest concentration of polygons in the 30°N-65°N study area is strongly correlated with below-average abundances of hydrogen and presumed near-surface ice (Figure 13).

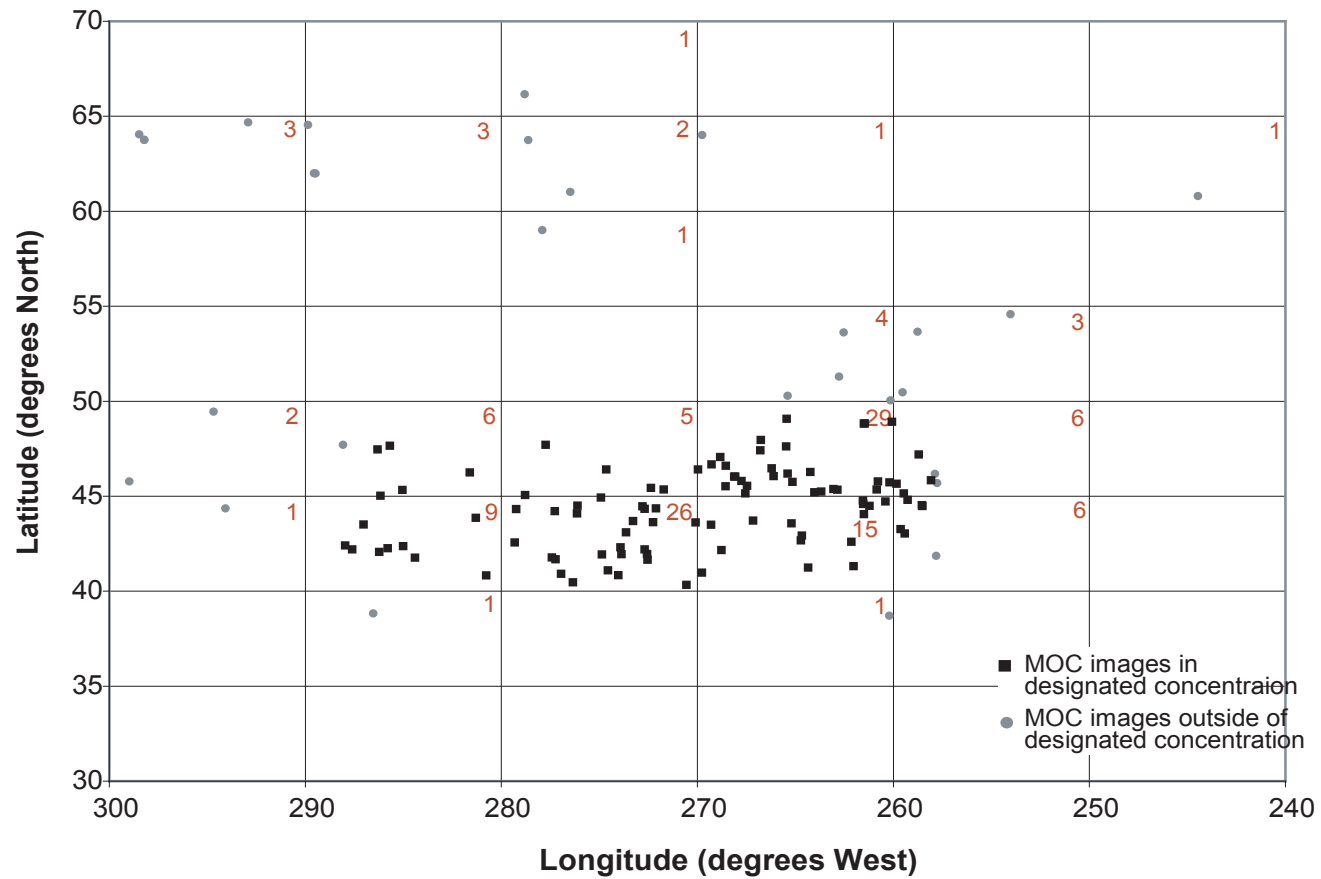


Figure 11. The locations of polygonal ground in the concentration (black squares) between 40°N-50°N and 258°W - 288°W in western Utopia Planitia of the Casius Quadrangle for 10 x 5 degree regions. The concentration represents 77% of the total 127 MOC images that reveal polygonal terrain in the Casius quadrangle. The numbers written in red in each quad corner represent the number of polygon-containing MOC images in that region.

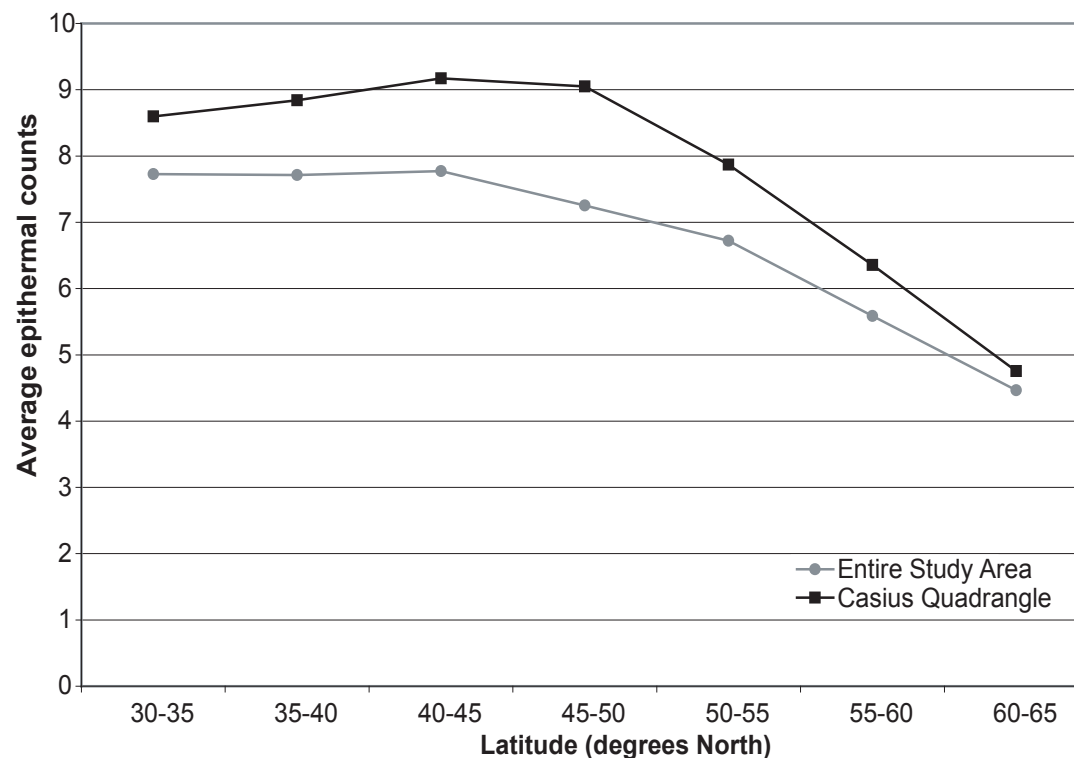


Figure 12. The average epithermal neutron flux rate data for ten degree latitude bands for the entire study area and the Casius Quadrangle. Flux rate data in 2 x 2 cells were used for the entire study area, whereas data in 0.05 x 0.05 cells were used for the Casius Quadrangle. Average values are given in the table. Because epithermal neutron flux rate data is inversely related to hydrogen, and thus water abundance (Boynton et al. 2002; Feldman et al. 2002), water-ice abundance of the entire study area and Casius Quadrangle increases poleward.

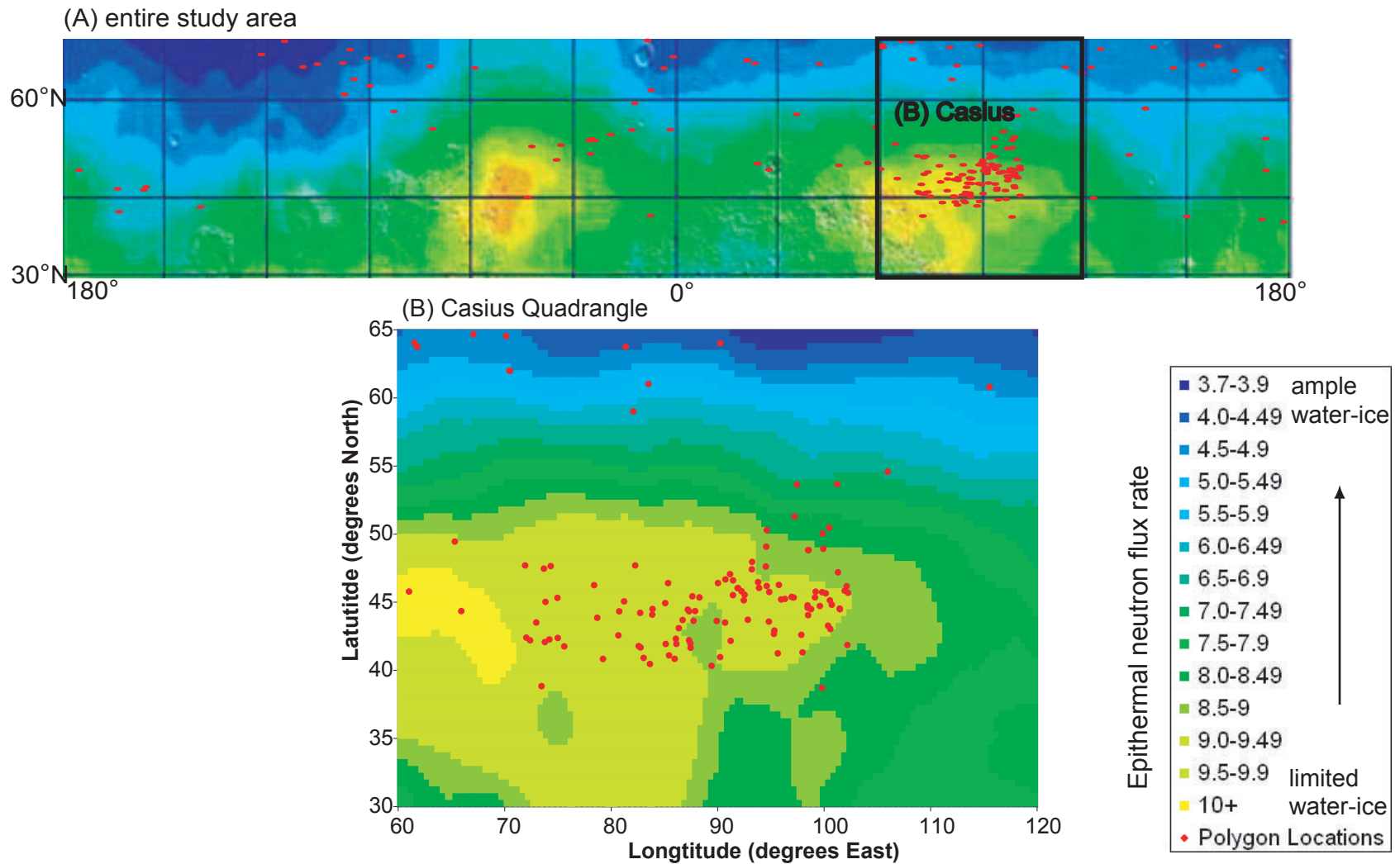


Figure 13. Location of polygonal terrain and epithermal neutron flux rates for (A) the entire study area and (B) the Casius Quadrangle. Because neutron flux rates are inversely related to hydrogen, and thus inferred water-ice, abundance, concentrations of polygonal terrain exist in areas of limited water-ice.



### *Geology and elevation*

The location of MOC images showing polygonal terrain corresponds to several geologic units of the lowland terrains and northern plains assemblages. Inclusive units are the smooth plains material and members of the Arcadia and Vastitas Borealis Formation (Greeley and Guest, 1987) (Table 2).

Table 2. Correlation between geologic units and location of polygonal terrain

Geologic Member	Age	Origin	# of MOC images revealing polygonal terrain (of 202) <sup>a</sup>
Smooth Plains Material (Aps)	Amazonian	aeolian	13
Arcadia Formation (Aa1)	Amazonian	volcanic	7
Vastitas Borealis Mottled (Hvm)	Late Hesperian	Volcanic, alluvial, or aeolian	71
Knobby (Hvk)			75
Plateau Sequence Cratered (Npl <sub>1</sub> )	Noachian	Volcanic, lava flows	7
Ridged (Nplr)			10
Southern Highlands	Noachian, Hesperian	Volcanic, aeolian	10

<sup>a</sup>Because exact latitude and longitude of geologic units was not available, corresponding locations of all MOC images are difficult to determine.

The concentration of polygonal terrain in the western Utopia Planitia region corresponds to the Vastitas Borealis Formation, the sub-polar plains deposits of the northern lowlands (Figure 14).

In broad comparison to topography, polygonal terrain exists at low elevations, < 0 km, and the concentration in the Casius Quadrangle exists west of the basin in Utopia Planitia (Figure 15). More specifically, elevation values range from -1.88 km to -6.438 km between 30°N-65°N, with an average value of -4.111 km. The majority, 168 of 202,

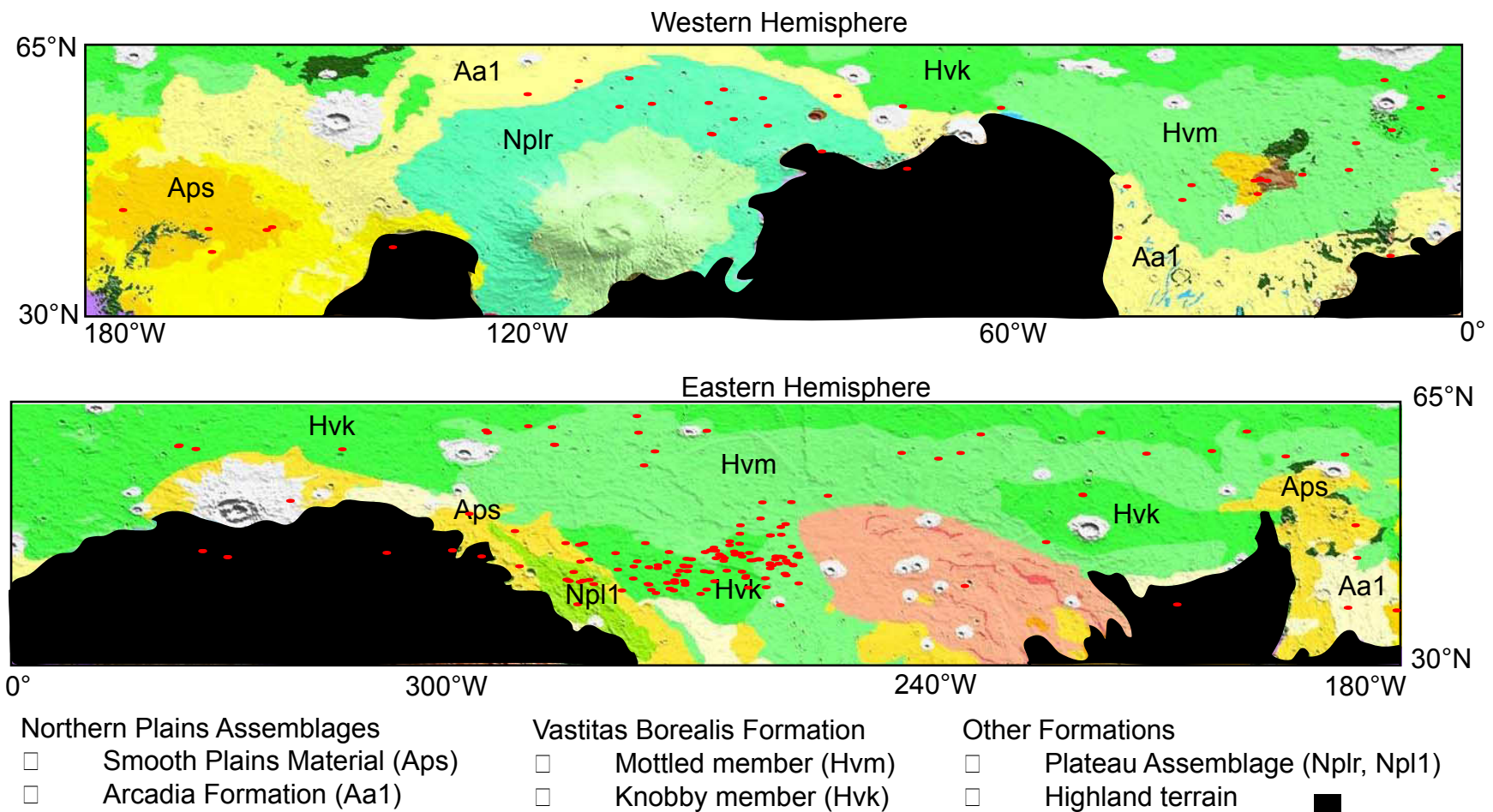


Figure 14. Location of polygonal terrain throughout the study are located in geologic units of diverse age and origin (modified from Greeley and Guest, 1987 and Tanaka et al., 1988). Because of the presence of polygonal terrain in a range of geologic units, the geologic units described in this map are not a primary factor in affecting polygon formation. See text for estimated number of MOC images in each geologic unit.

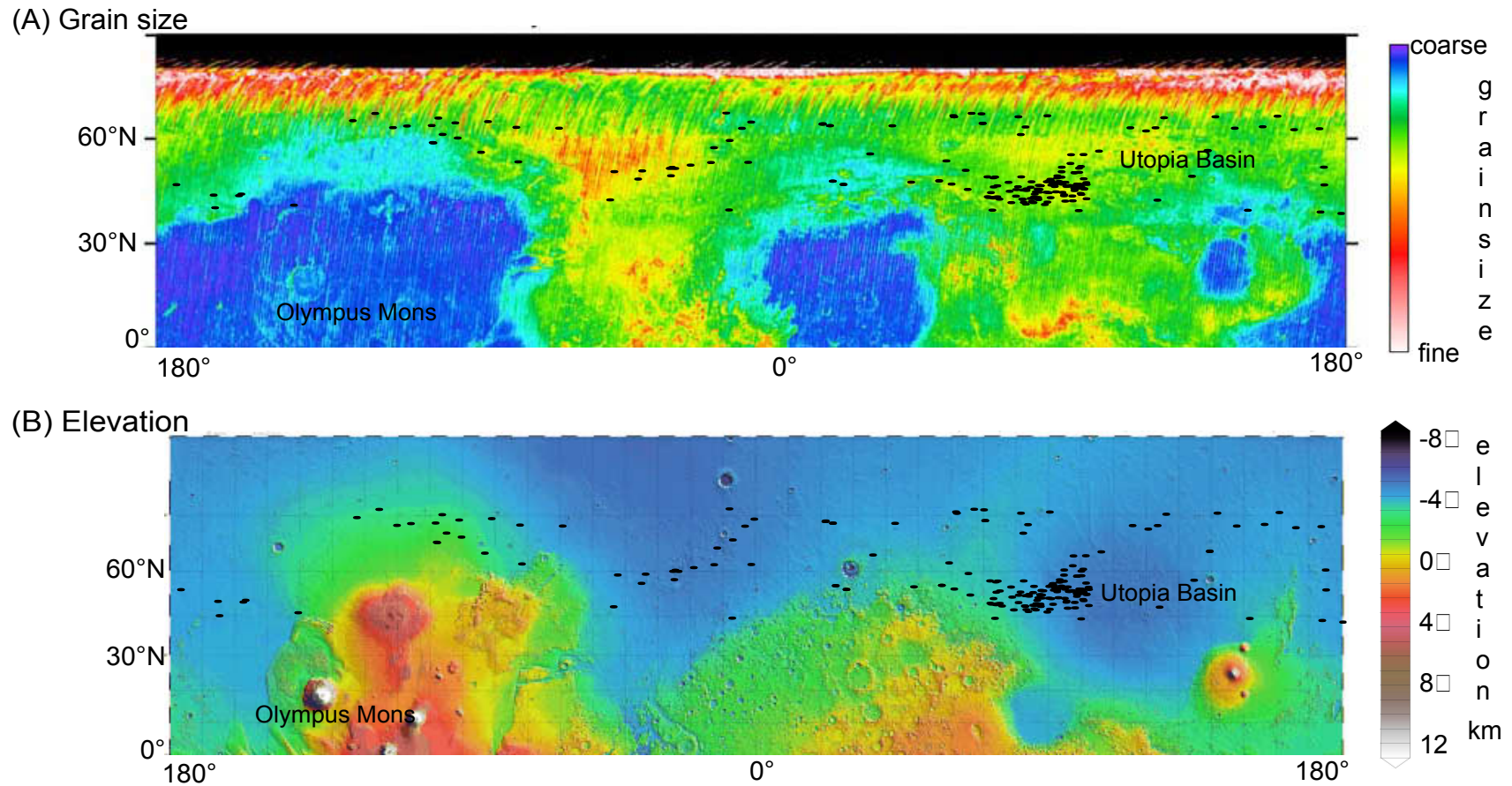


Figure 15. Comparison of polygon location to thermal inertia and topography. (A) Polygonal terrain is present in areas where thermal inertia values indicate medium grain size. (B) Polygonal terrain exists at low elevations  $< 0$  km, but is not concentrated at the lowest elevations, such as the Utopia basin. Maps courtesy of <http://argyre.colorado.edu/inertia/smap2003.jpg> and <http://ltpwww.gsfc.nasa.gov/tharsis/global.map.html>

or 83%, of the images exist at elevations between -3.5 km to -5.0 km. Polygonal terrain corresponds to thermal inertia values indicative of medium grain size (Figure 16).

#### *Albedo and geometry of polygons*

For the entire study area, the locations of sublimation polygons are restricted to 40°N-55°N, icy polygons are constrained to 55°N-65°N, and intermediate polygons exist at all latitudes, 30°N-65°N (Figure 17). Between 40°N-55°N, 66 % of the 141 MOC images show sublimation polygons and 73 % of the MOC images at latitudes between 55°N-65°N show icy polygons (Appendix 3, Table A2). The following generalizations can be made about polygon geometry: low-latitude polygons are well-defined and often reveal a rectilinear geometry and linear orientation trending north-south. In comparison, polygonal networks at high latitudes often exhibit rectilinear and hexagonal geometry and are located within crater boundaries that trend in a similar circular pattern to that of the crater rim.

#### *Preferred orientation and the auto-correlation function*

In 53% of MOC images revealing the presence of polygon terrain, patterns exhibit a preferred orientation --- longest edges of the polygons run parallel and strike north-south --- and a secondary orientation, perpendicular to that of the primary. ACF projections verify this primary axis trending north-south and show secondary axis trending east-west (Figure 18). Trends of the primary axis vary from 78° to 94° north of east, with an average value of 88° north of east (Appendix 4, Table A3). Elevation values for ACF images range from -3.516 km to -4.834 km and elevation for the selected area

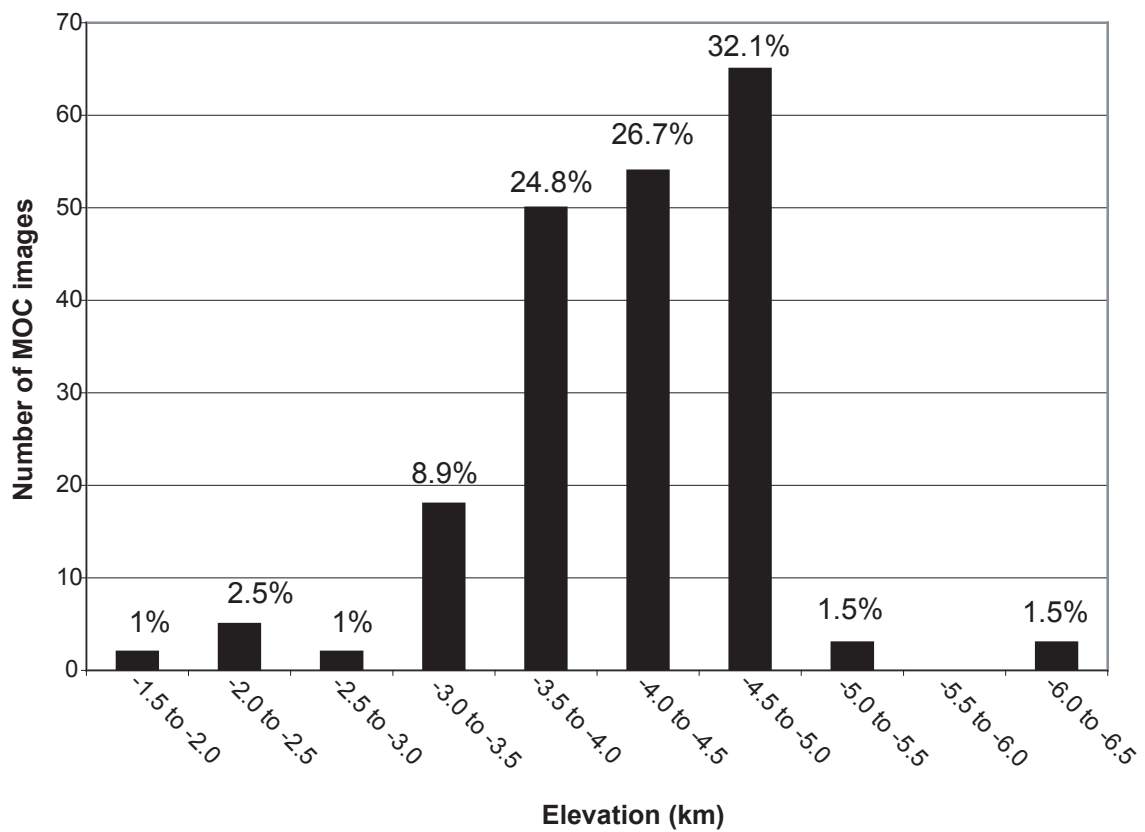
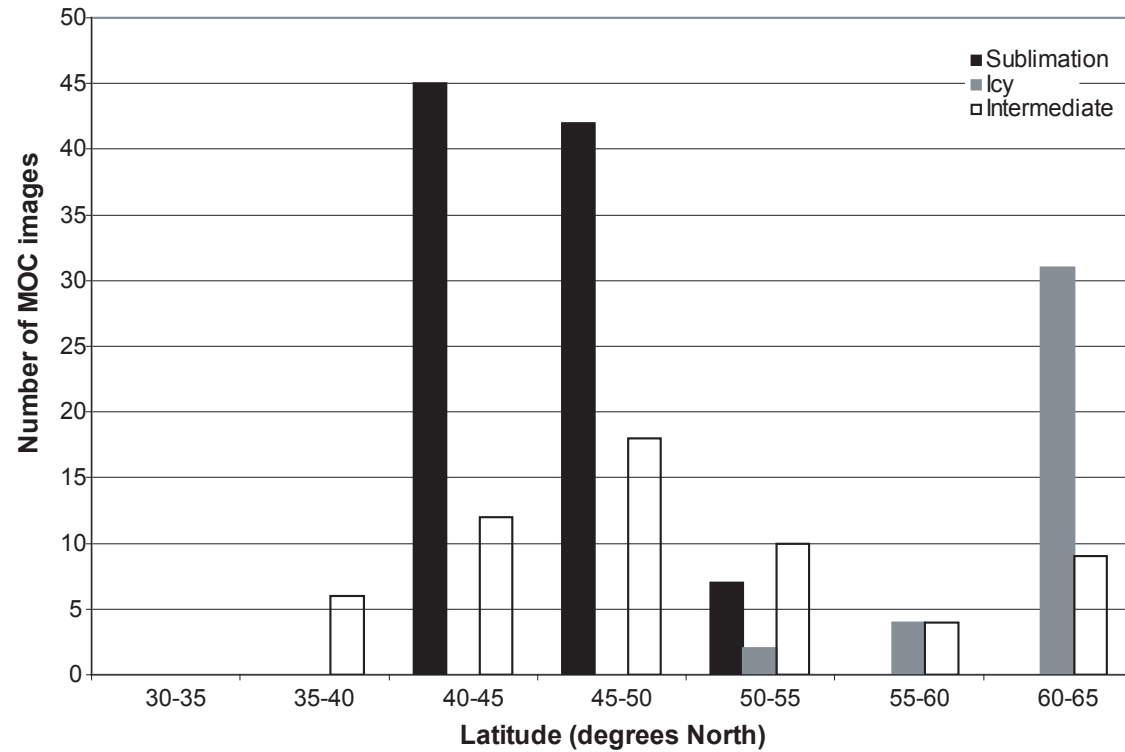


Figure 16. Topographic distribution of all MOC images that reveal polygonal terrain between 30°N and 65°N. Elevation values range more than 4.5 km, from -1.88 km to -6.438 km. Eight-three percent of all MOC images are located at elevations between -3.5 km and -5.0 km.



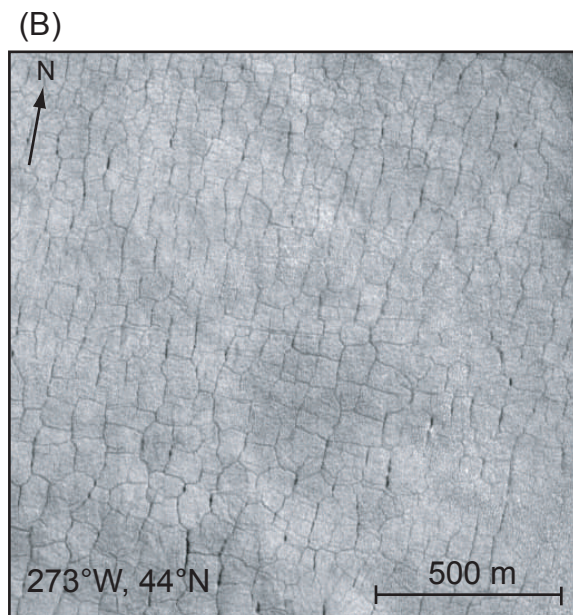
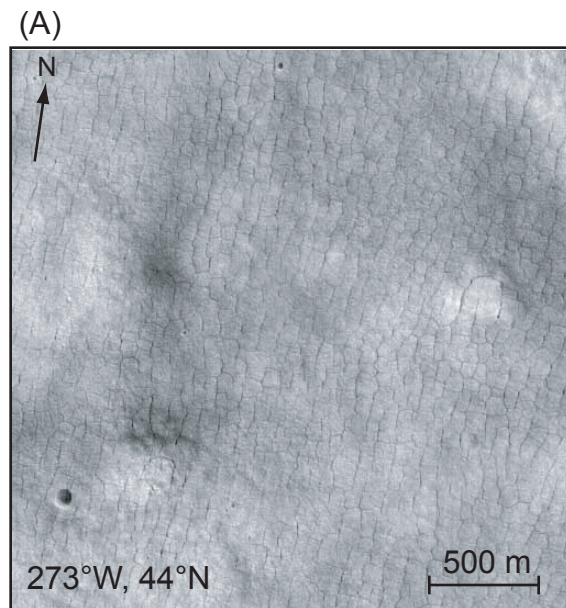
Number of MOC images

Latitude (°N)	30 -35	35-40	40-45	45-50	50-55	55-60	60-65
Sublimation	0	0	45	42	7	0	0
Icy	0	0	0	0	2	4	31
Intermediate	0	6	12	18	10	4	9

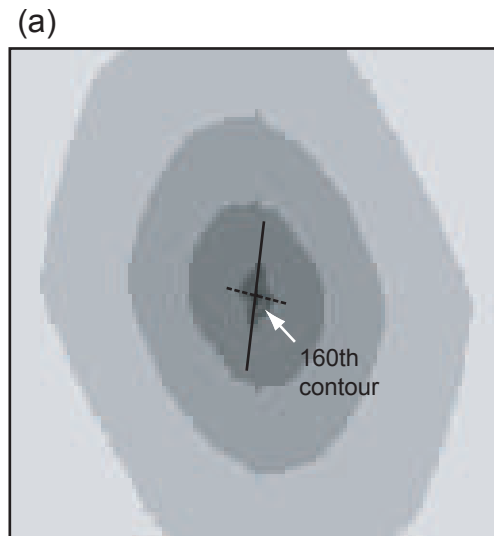
Figure 17. Number of sublimation, icy, and indiscriminate polygons in five degree latitude zones for the entire study area. The 40°N and 55°N latitude lines acts as transition zones for sublimation and icy polygons. Sublimation polygons are restricted to latitudes 40°N - 55°N, while icy polygons are constrained to latitudes north of 55°N.



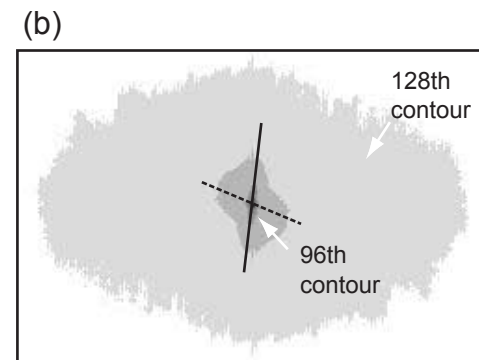
## MOC images



## ACF Images



Angle  $\sim 86^\circ$  counterclockwise from horizontal



Angle  $\sim 85^\circ$  counterclockwise from horizontal

Figure 18. Quantification of the preferential orientation of polygonal terrain in western Utopia Planitia using the auto-correlation function, ACF. Original selections of MOC images (A) M0401631 and (B) M0304331, and their corresponding ACF images (a), (b). The primary axis that trends north-south is apparent in both the MOC and ACF image, and can be quantified in the ACF image. Both images also reveal a secondary trend  $\sim 90^\circ$  from the primary axis as indicated by the dashed line. Description of contours is given in Appendix 1.

that includes all ACF images, defined by the coordinates 40°N to 50°N and 256°N to 290°N decreases moving east along lines of longitude (Figure 19A). Comparison of the two-fold orientation to topography reveals that the primary orientation follows topographic contours while the secondary orientation trends perpendicular to topography (Figure 19B).

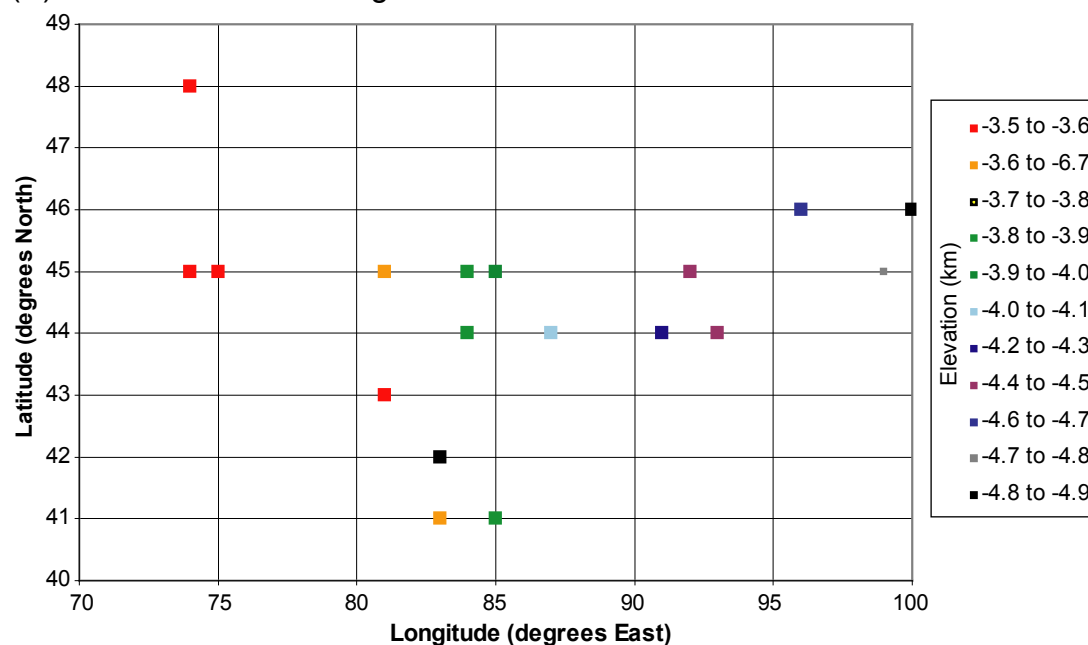
## **Discussion**

The presence of geomorphic ice features at all latitudes within the study area illustrates that water once existed, and perhaps still exists, in the Martian subsurface. Assuming Martian polygons are truly analogous to terrestrial polygons, the locations of Martian polygon areas where there is now limited ice in the shallow subsurface suggests that there must have been ice in the Martian near-surface that is not there now. More detailed studies of the location of polygonal terrain with respect to topography, geology, and geometry of polygons imply that the behavior of polygonal terrain on Mars is similar to the behavior of terrestrial polygons. The color, as seen in the albedo of the troughs, provides further indication that at low latitudes ice has sublimed away and at high latitudes ice may still be present. In its entirety, these inferences indicate a change in Martian climate, resulting in the loss of ice at mid-latitudes on Mars.

Indication that polygon morphology has persisted, despite loss of ice, can be seen in the appearance of the polygons themselves. Polygonal terrain characterized by darkly-shaded troughs only exists at latitudes between 35°N and 55°N. It is possible that this appearance indicates a dust lag resulting from the sublimation of trough ice. In stark contrast, polygonal terrain located between 55°N-65°N is distinguished by highly



(A) Elevation of ACF images at 100 m intervals



(B) Elevation and polygon orientation

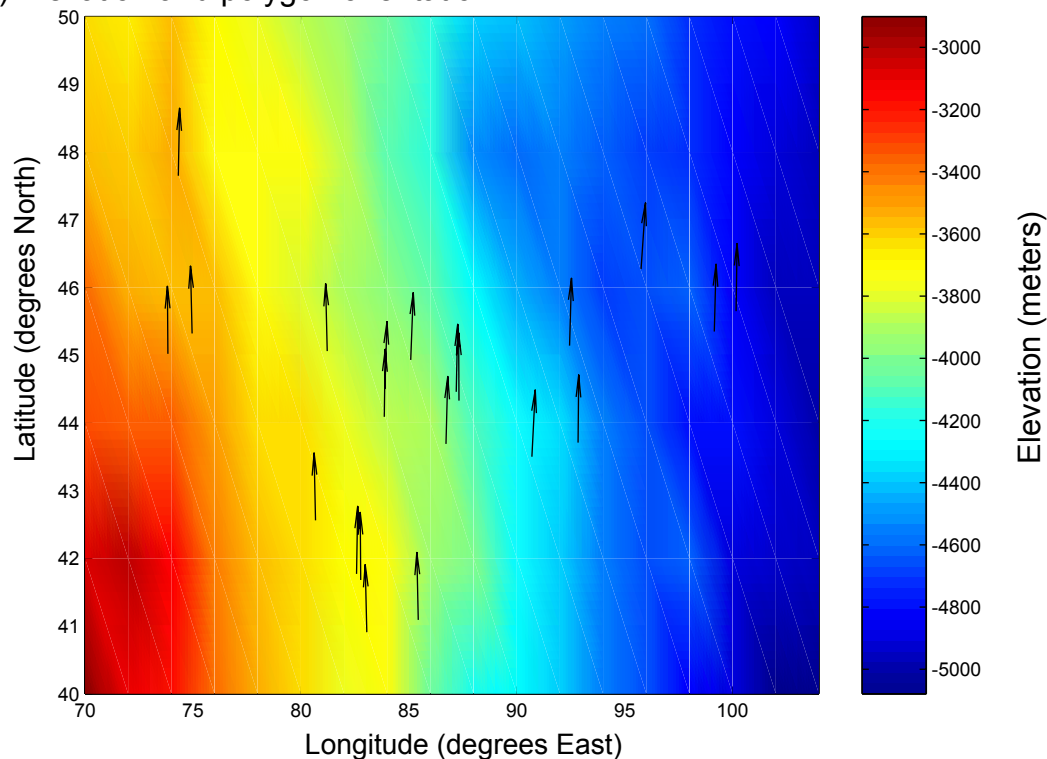


Figure 19. (A) Specific elevations of MOC images used in ACF analysis. Topographic variations decrease eastward. (B) Relationship between elevation and polygon orientation. Preferred orientation is parallel to topographic contour, thus secondary orientation (not depicted above) is perpendicular to topography for this region in western Utopia Planitia.

reflective troughs. It is possible that this bright material in the troughs indicates substantially more near-surface water-ice than is found in the darker polygons to the south. This appearance of Martian polygonal terrain has terrestrial analogs.

In Antarctic and Arctic permafrost regions, studies show analogous sublimation of near-surface ice in the uppermost meter. In Beacon Valley, Antarctica, cosmogenic isotope studies of granitic till superimposed on ice-wedge polygons provides strong evidence that the till is a lag deposit sourced from a glacial advance (Marchant et al., 2002). Marchant et al. (2002) indicate that although water-ice is not currently present in polygon troughs, it did exist in the near subsurface at the time of formation and the morphology of polygons is still preserved through warming periods, including sublimation of overlying ground ice. Furthermore, in northern Quebec, radiocarbon dating of ice-wedges indicates that significant thawing has occurred during at least the last two kyr, resulting in unusually deep troughs between polygons (Gray and Seppala, 1991). This study shows that while polygon growth may be inactive today, their morphology can be preserved for thousands or millions of years through significant thawing of ice-wedges. These studies indicate that polygonal terrain on Earth can exist in areas of limited near-surface ice.

The comparison of high-energy spectroscopy data and MOC images also shows poor correlation between the distribution of near-surface water-ice and the location of polygons. Polygons are present in areas of both low and high concentrations of water-ice and the high concentration of polygonal ground in the Casius Quadrangle is located in an area of limited near-surface water-ice. Furthermore, sublimation polygons correlate with areas of limited water ice and icy polygons exist in areas of more abundant water-ice

(Figure 20). These locations suggest that polygons at mid-northern latitudes formed at a time when near-surface ice was present and that the morphology has persisted even though near-surface ice is not stable there today.

Since it is not the present distribution of subsurface water-ice that controls polygon location, it is helpful to further examine other surface components that may influence polygon location and formation. While all polygonal terrain at mid-northern latitudes occurs at low elevation ( $< 0$  km) polygonal terrain is not associated with areas, such as the Utopia Basin, that are at the lowest elevation of the study area. This relationship argues against the hypothesis that the collection of water and water-ice at the lowest elevations would favor polygon formation. In addition, the distribution of polygonal terrain across several geologic units of diverse age and origin also suggests that the composition of surface bedrock does not obviously influence polygon development. This non-correlation is consistent throughout the  $30^{\circ}\text{N}$ - $65^{\circ}\text{N}$  latitudinal band as well as within the concentration in the Casius Quadrangle. Neither topography nor geology obviously influences polygon distribution.

However, the geometry of Martian polygons appears similar to terrestrial polygons, which may have implications for polygon distribution. The majority of MOC images revealing polygonal terrain also show polygonal patterns that have a preferential orientation trending north-south. Quantification of this orientation in the Casius Quadrangle shows that the primary orientation follows topographic contours in the area and the secondary orientation trends perpendicular to topography. This relationship between polygon orientation and topography is analogous to the alignment of terrestrial polygons and topography (Mackay, telephone communication). Because terrestrial

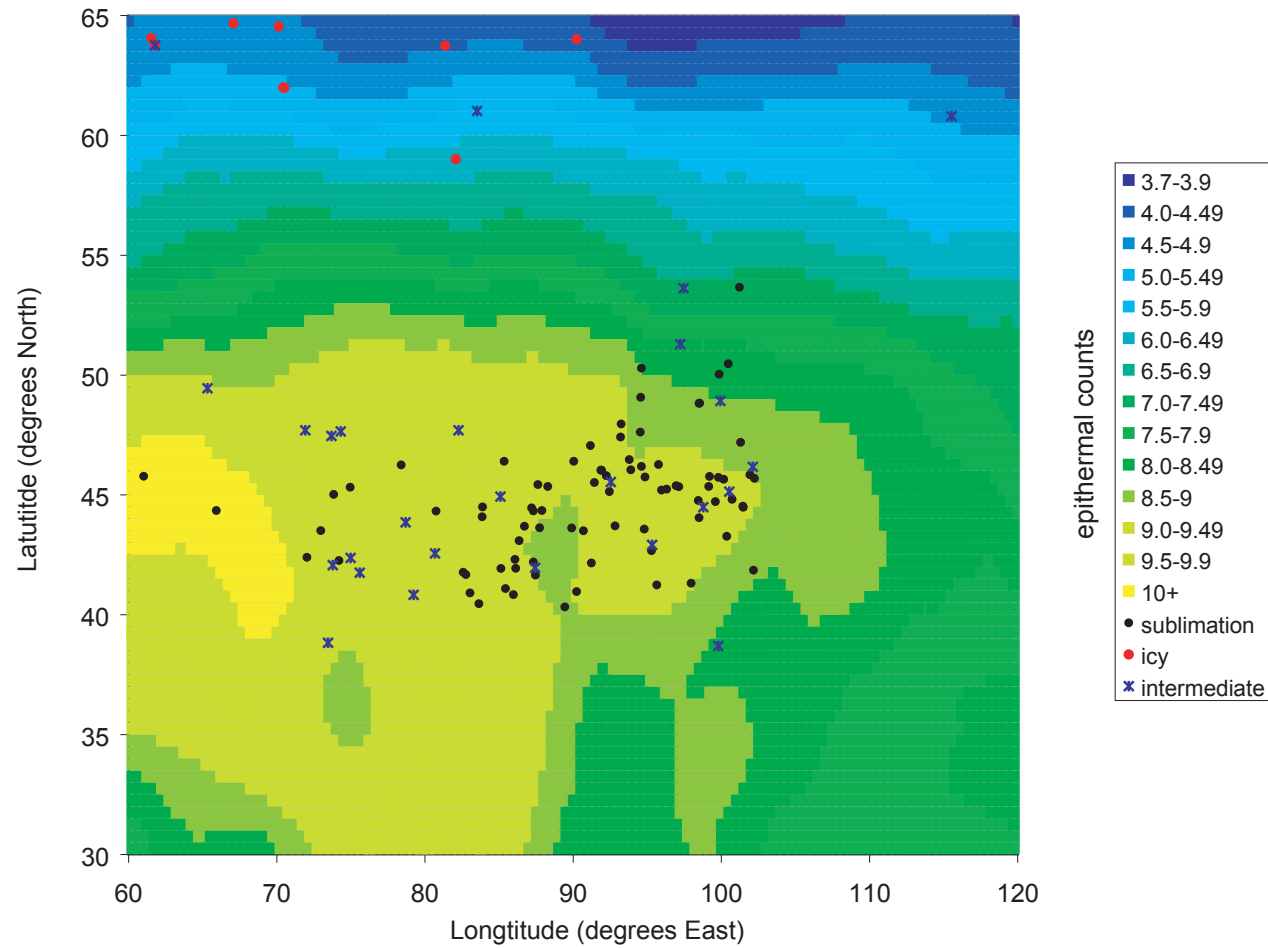


Figure 20. Relationship between polygon albedo and hydrogen abundance. Polygons that indicate sublimation of near-surface water-ice are located in areas of limited water-ice. Polygons that reveal a greater abundance of water-ice also exist in regions where spectroscopy data indicates a great abundance of near surface water ice.

polygon alignment is also linked with ancient shorelines, it is possible that the Martian polygons developed in response to an ancient shoreline. Such shorelines may be associated with the Heisinger and Head (2000) hypothesis that ancient bodies of water were once located in the Utopia Basin.

A further indication that the Martian polygons behave in a similar way to terrestrial polygons is the similarity in the polygon shape. Although the geometry of individual polygons was not objectively quantified for this study, there appears to be a relationship between polygonal shape, either rectangular or hexagonal, and latitude. The majority of polygons at mid latitudes, 30°N-55°N, appear to have four sides with preferential orientations north-south and east-west. The majority of polygons at high latitudes, 55°N-65°N, appear to have more than four sides. Because the combination of field studies and modeling of terrestrial polygons show that younger polygons are linked with rectangular geometry and older polygons are associated with hexagonal geometry (Plug and Werner, 2001), similar geometry of the Martian polygons may also indicate their relative length of time of active development. High latitude hexagonal polygons on Mars may have developed for a longer duration of time, and perhaps are even still active, than the low latitude, rectangular polygons.

Data from this study support the hypothesis that polygons located at mid-northern latitudes formed under a previous Martian climate. The presence of small-scale polygonal terrain on Mars is indicative of stable water-ice at some point, past or present, in Martian climate history. Because neutron and gamma-ray spectrometers record hydrogen abundance in the uppermost meter of the Martian subsurface, spectroscopy data is indicative of stable ice in that layer today. Thus, if there is a global correspondence

between polygonal terrain and hydrogen abundance, polygons are likely in equilibrium with current climate. If polygons exist in areas with little ground ice today, then these polygons may have formed under earlier climatic conditions that favored water-ice stability. Location data from this study show that polygons do exist in areas of limited water-ice. Albedo comparisons also show that polygons at latitudes between  $35^{\circ}\text{N}$ -  $55^{\circ}\text{N}$  are analogous to sublimation polygons, which lack near subsurface ice, and polygons at latitudes between  $55^{\circ}\text{N}$ -  $65^{\circ}\text{N}$  indicate the presence of subsurface ice. Thus, the combination of polygon distribution and appearance show latitudinal variation in ice stability in a previous geologic time. The dominant factor thought to control latitudinal variations in ice stability is the obliquity of Mars' orbit.

Theoretical models show that at the present obliquity of  $25^{\circ}$  water-ice is stable poleward of  $\sim 55^{\circ}$ . At high obliquities of  $35^{\circ}$  to  $45^{\circ}$ , water-ice is stable at mid latitudes and even equatorial regions (Mellon and Jakosky, 1993; Mischna et al., 2003). Models also show that Mars has reached these high obliquities during the recent past. Between about 2,100 and 400 kyr Mars's obliquity varied around and often exceeded  $30^{\circ}$ , moving the stability of water-ice equatorward. However, within the past  $\sim 300$  kyr, obliquity has remained at  $25^{\circ}$  with comparatively little variation, resulting in the stability of water-ice poleward of  $\sim 55^{\circ}$  (Head et al., 2003). While warming periods have removed much of the ice up to one meter depth, it has taken longer to remove ice at depths greater than one meter. Thus, it is possible that polygonal terrain is at least 300 kyr old and formed during the latest period of high obliquity. Head et al., (2003) has interpreted the stage of high obliquity as a glacial period, when there is thought to be a net deposition of water-ice at mid-latitudes. The removal of ice at mid-latitudes during periods of low obliquity is

interpreted as an interglacial period (Head et al., 2003). The concentrations of small-scale polygonal terrain at mid-latitudes in areas where spectroscopy data reveals limited abundance of water-ice supports the hypothesis that the current climate may represent an interglacial period where water-ice is only stable poleward of  $50^\circ$  and that a previous climate may represent a glacial period where water-ice is stable poleward of  $30^\circ$ .

## Summary

This study demonstrates that small-scale polygons on Mars develop analogous to terrestrial ice-wedge polygons and suggests the location of Martian polygonal terrain in areas of limited near-surface water ice is indicative of Martian climate change. The six conclusions described below are consistent with polygonal terrain formation during periods of higher obliquity and in conjunction with equatorward stability of water-ice. As obliquity decreased, ice sublimed, leaving polygonal morphology at the surface and relict polygons below the one-meter sampling depth of high-energy spectrometers.

(1) Polygonal terrain is found at all latitudes in the study area,  $30^\circ\text{N}$  to  $65^\circ\text{N}$  including regions where spectroscopy indicates little to no water-ice in the uppermost meter of the Martian subsurface.

(2) Polygons in the ice-poor regions have low albedo, indicationing that surface ice has sublimed away.

(3) Polygonal terrain exists at low elevations,  $< 0$  km, in the mid-northern mid latitudes, but not in the areas of lowest elevations, like the Utopia basin.

(4) Polygonal terrain is found in a variety of geologic units of diverse age and origin.

(5) Polygonal terrain is located in areas of medium grain size as indicated by thermal inertia values.

(6) The primary orientation of polygonal terrain in the Casius Quadrangle trends generally north-south and is parallel to topographic contours; a secondary orientation is trends perpendicular to the primary orientation and thus topography.



## **Acknowledgements**

Many thanks go to Carlton Allen and Mary Sue Bell, of NASA Johnson Space Center, for proposing the project, for their guidance in the methods and analysis, and for their mentorship throughout; especially to Sara Mitchell for reviewing drafts and challenging me to become a better writer; to William Boynton and William Feldman for the spectroscopy data; to Ralph Milliken for the MOLA topography data; to Dave Bice for helpful advising, and for guidance with MatLab; to Cam Davidson for the introduction to the auto-correlation function; to Alison Anders for arranging a visit to the University of Seattle; and to Bre MacInnes and Leah Morgan for their company and support in Northfield, San Francisco, and Italy. This study was funded by the Universities Space Research Association and the Bernstein Student Research Endowment.

## References Cited

- Allen, C. C., 1979, Volcano-Ice Interactions on Mars: *Journal of Geophysical Research*, v. 84, p. 8048-8059.
- Boynton, W., 2004, e-mail communication: Johnson Space Center Houston.
- Boynton, W. V., Feldman, W. C., Squyres, S. W., Prettyman, T. H., Bruckner, J., Evans, L. G., Reedy, R. C., Starr, R., Arnold, J. R., Drake, D. M., Englert, P. A. J., Metzger, A. E., Mitrofanov, I., Trombka, J. I., d'Uston, C., Wanke, H., Gasnault, O., Hamara, D. K., Janes, D. M., Marcialis, R. L., Maurice, S., Mikheeva, I., Taylor, G. J., Tokar, R., and Shinohara, C., 2002, Distribution of hydrogen in the near surface of Mars: Evidence for subsurface ice deposits: *Science*, v. 297, no. 5578, p. 81-85.
- Brook, G. A., 1982, Ice wedge polygons, Baydjarakhs, and alases in Lunae Planum: NASA Technical Memorandum, no. 85127, p. 265-267.
- Carr, M. H., and Schaber, G. G., 1977, Martian Permafrost Features: *Transactions-American Geophysical Union*, v. 58, no. 8, p. 829-829.
- Christensen, P. R., and Moore, H. J., 1992, The Martian Surface Layer, *in* Kieffer, H. H., Jakosky, B. M., Snyder, C. W., and Matthews, M. S., eds., *Mars*: Tuscon, The University of Arizona Press.
- Clifford, S. M., and Hillel, D., 1983, The Stability of Ground Ice in the Equatorial Region of Mars: *Journal of Geophysical Research*, v. 88, no. NB3, p. 2456-2474.
- Davidson, C., Rosenberg, C., and Schmid, S. M., 1996, Synmagmatic folding of the base of the Bergell pluton, Central Alps: *Tectonophysics*, v. 265, p. 213-238.
- Evans, N. E., and Rossbacher, L. A., 1980, The last picture show: small-scale patterned ground in Lunae Planum: NASA Technical Memorandum, no. 82385, p. 376-378.
- Fanale, F. P., Postawko, S. E., Pollack, J. B., Carr, M. H., and Pepin, R. O., 1992, Mars: Epochal Climate Change and Volatile History, *in* Kieffer, H. H., Jakosky, B. M., Snyder, C. W., and Matthews, M. S., eds., *Mars*: Tuscon, The University of Arizona Press, p. 1536.
- Farmer, C. B., and Doms, P. E., 1979, Global and seasonal variation of water vapor on Mars and the implications for permafrost: *Journal of Geophysical Research*, v. 84, p. 2881-2888.
- Feldman, W. C., Boynton, W. V., Tokar, R. L., Prettyman, T. H., Gasnault, O., Squyres, S. W., Elphic, R. C., Lawrence, D. J., Lawson, S. L., Maurice, S., McKinney, G. W., Moore, K. R., and Reedy, R. C., 2002, Global distribution of neutrons from Mars: Results from Mars Odyssey: *Science*, v. 297, no. 5578, p. 75-78.
- Gray, J. T., and Seppala, M., 1991, Deeply Dissected Tundra Polygons on a Glacio-Fluvial Outwash Plain, Northern Ungava Peninsula, Quebec: *Geographie Physique Et Quaternaire*, v. 45, no. 1, p. 111-117.
- Greeley, R., and Guest, J. E., 1987, Geologic Map of the Eastern Equatorial Region of Mars: U.S. Geological Survey Miscellaneous Investigations Series Map I-1802-B.

- Hartmann, W. K., and Neukum, G., 2001, Cratering Chronology and the Evolution of Mars: *Space Science Reviews*, v. 96, no. 1/4, p. 165-194.
- Head, J. W., Mustard, J. F., Kreslavsky, M. A., Milliken, R. E., and Marchant, D. R., 2003, Recent ice ages on Mars: *Nature*, v. 426, no. 6968, p. 797-802.
- Helfenstein, P. H., and Mouginis-Mark, P. J., 1980, Morphology and distribution of fractured terrain on Mars, *in* Lunar and Planetary Science Conference XI, p. 429-439.
- Hiesinger, H., and Head, J. W., 2000, Characteristics and origin of polygonal terrain in southern Utopia Planitia, Mars: Results from Mars Orbiter Laser Altimeter and Mars Orbiter Camera Data: *Journal of Geophysical Research-Planets*, v. 105, no. E5, p. 11999-12022.
- Kerfoot, D. E., 1972, Thermal contraction cracks in an arctic tundra environment: *Arctic*, v. 25, no. 2, p. 142-150.
- Kieffer, H. H., and Zent, A. P., 1992, Quasi-Periodic Climate Change on Mars, *in* Kieffer, H. H., Jakosky, B. M., Snyder, C. W., and Matthews, M. S., eds., Mars: Tuscon, The University of Arizona Press, p. 1536.
- Lachenbruch, A. H., 1962, Mechanics of thermal contraction cracks and ice-wedge polygons in permafrost: *Special Paper - Geological Society of America*, v. 69.
- Mackay, J. R., 1995, Ice wedges on hillslopes and landforms evolution in the late Quaternary, western Arctic coast, Canada: *Canadian Journal of Earth Sciences*, v. 32, p. 1093-1105.
- Mackay, J.R., 2004, telephone communication: Northfield.
- Mackay, J. R., and Burn, C. R., 2002, The first 20 years (1978-1979 to 1998-1999) of ice-wedge growth at the Illisarvik experimental drained lake site, western Arctic coast, Canada: *Canadian Journal of Earth Sciences*, v. 39, no. 1, p. 95-111.
- Malin, M. C., Edgett, K. S., Carr, M. H., Danielson, G. E., Davies, M. E., Hartmann, W. K., Ingersoll, A. P., James, P. B., Masursky, H., McEwen, A. S., Soderblom, L. A., Thomas, P., Ververka, J., Caplinger, M. A., Ravine, M. A., Soulanille, T. A., and Warren, J. L., 2003-2004, NASA's Planetary Photojournal.
- Mangold, N., 2003, Distribution and Climatic Control of Small Scale Polygons on Mars, *in* Third Mars Polar Science Conference, Alberta, Canada, Abstract #8044.
- Mangold, N., Maurice, S., Feldman, W. C., Costard, F., and Foget, F., 2003, Geographical Relationships Between Small Scale Polygons and Ground Ice Distribution From Neutron Spectrometer on Mars, *in* Third Mars Polar Science Conference, Alberta, Canada, Abstract #8043.
- Marchant, D. R., Lewis, A. R., Phillips, W. M., Moore, E. J., Souchez, R. A., Denton, G. H., Sugden, D. E., Potter, N., and Landis, G. P., 2002, Formation of patterned ground and sublimation till over Miocene glacier ice in Beacon Valley, southern Victoria Land, Antarctica: *Geological Society of America Bulletin*, v. 114, no. 6, p. 718-730.

- Mellon, M. T., 1997, Small-scale polygonal features on Mars: Seasonal thermal contraction cracks in permafrost: *Journal of Geophysical Research-Planets*, v. 102, no. E11, p. 25617-25628.
- Mellon, M. T., and Jakosky, B. M., 1993, Geographic Variations in the Thermal and Diffusive Stability of Ground Ice on Mars: *Journal of Geophysical Research-Planets*, v. 98, no. E2, p. 3345-3364.
- Milliken, R. E., 2004, e-mail communication: Northfield.
- Mischna, M. A., McCleese, D. J., Richardson, M. I., Vasavada, A. R., and Wilson, R. J., 2003, Volatile Cycling and Layering on Mars: Observations, Theory and Modeling, *in* Sixth International Conference on Mars, Pasadena, California, Abstract #3145.
- Mitrofanov, I., Anfimov, D., Kozyrev, A., Litvak, M., Sanin, A., Tret'yakov, V., Krylov, A., Shvetsov, V., Boynton, W., Shinohara, C., Hamara, D., and Saunders, R. S., 2002, Maps of subsurface hydrogen from the high energy neutron detector, Mars Odyssey: *Science*, v. 297, no. 5578, p. 78-81.
- Morris, E. C., and Underwood, J. R., 1978, Polygonal fractures of the martian plains: NASA Technical Memorandum, v. 79729, p. 97-99.
- Mouginis-Mark, P. J., 1979, Martian fluidized crater morphology: Variations with crater size, latitude, altitude, and target material: *Journal of Geophysical Research*, v. 84, p. 8011-8022.
- Mutch, T. A., Arvidson, R. E., Binder, A. B., Guinness, E. A., and Morris, E. C., 1977, The Geology of the Viking Lander 2 Site: *Journal of Geophysical Research*, v. 82, no. 28, p. 4452-4467.
- Paige, D. A., 1992, The thermal stability of near-surface ground ice on Mars: *Nature*, v. 356, p. 43-45.
- Panozzo, H. R., 1992, The auto correlation function: an image processing tool for fabric analysis: *Tectonophysics*, v. 212, p. 351-370.
- Pechmann, J. C., 1980, The Origin of Polygonal Troughs on the Northern Plains of Mars: *Icarus*, v. 42, no. 2, p. 185-210.
- Plug, L. J., and Werner, B. T., 2001, Fracture networks in frozen ground: *Journal of Geophysical Research-Solid Earth*, v. 106, no. B5, p. 8599-8613.
- Pratt, W. E., 1958, Large-scale polygonal jointing: *Bulletin of the American Association of Petroleum Geologists*, v. 42, no. 9, p. 2249-2251.
- Putzig, N. E., Mellon, M. T., and Arvidson, R. E., 2003, Thermophysical properties of the Martian south polar region, *in* Sixth International Mars Conference, Lunar and Planetary Institute, Houston.
- Seibert, N. M., and Kargel, J. S., 2001, Small-scale Martian polygonal terrain: Implications for liquid surface water: *Geophysical Research Letters*, v. 28, no. 5, p. 899-902.

- Sletten, R. S., Hallet, B., and Fletcher, R. C., 2003, Resurfacing time of terrestrial surfaces by the formation and maturation of polygonal patterned ground: *Journal of Geophysical Research-Planets*, v. 108, no. E4.
- Tanaka, K. L., Scott, D. H., and Greeley, R., 1992, Global Stratigraphy, *in* Kieffer, H. H., Jakosky, B. M., Snyder, C. W., and Matthews, M. S., eds., *Mars*: Tuscon, The University of Arizona Press.
- Wechsler, A. E., and Glaser, P. E., 1965, Pressure effects on postulated lunar materials: *Icarus*, v. 4, p. 335-352.

### Appendix 1: The auto-correlation function (ACF)

The ACF is calculated using Fast Fourier Transform algorithms, defined by the following equation:

$$f(x, y) \otimes f(x, y) \\ = \int_{-\infty}^{\infty} \int_{-\infty}^{\infty} f(x', y') \bullet f(x + x', y + y') dx' dy'$$

where  $f(x, y)$  is the two-dimensional brightness function that defines the image,  $\otimes$  is the operation denoting a convolution or correlation, and  $x'$  and  $y'$  are the variables of integration (Panozzo, 1992).

The ACF displays the fabric orientation of an image by straining a generic circle in the directions of preferred orientation and feature extension. Because the ACF is dependent on brightness and cannot select objects of interest, it determines correlations and trends in albedo at different scales. That is, the ACF might express the orientation of the polygon troughs at one scale and the shadows produced by topographic variations at another scale. The ACF accounts for the preferred orientations at different scales through the use of contours: high-numbered contours are a function of small-scale features, while low-numbered contours are of function large-scale features. ACF contours range from 1 to 256 and the highest contours are located in the center of the ACF and decrease outward in all directions. Because polygonal troughs are small-scale features with respect to the image, determination of the angle orientation at high-numbered contours of 96, 128, and 160 are practical for this study.

## Appendix 2

Table A1. Mars Orbital Camera (MOC) images that reveal polygonal terrain

Quadrangle	MOC image Number	Latitude (degrees North)	Longitude (degrees West)
<i>Diacria</i>	E1201716	43.11	155.6
	E1202507	42.69	156.32
	FHA00694	45.62	175.4
	M0001948	40.16	139.54
	M1501063	39.46	163.6
	M1801140	42.85	164.06
	M2200677	62.7	121.6
<i>Arcadia</i>	E0100508	58.07	89.67
	E0301639	65.04	108.1
	E0400073	64.64	114.82
	E0502689	51.72	71.17
	E1101784	56.77	97.03
	E1501561	62.45	80.42
	M0200976	59.03	94.22
	M0200978	63.39	95.55
	M0204284	60.93	71.73
	M1900018	61.41	97.54
	M2000659	56.86	97.24
	M2000948	62.12	90.34
	M2101277	61.28	105.09
	M2201038	54.27	82.5
	M2301007	60.85	109.38
<i>Mare Acidalium</i>	E0300154	50.84	18.62
	E0300457	60.7	58.68
	E0501785	50.08	24.22
	E0502677	49.1	41.9
	E1300642	51.54	12.41
	E1700211	47.12	34.57
	E1700671	49.95	23.26
	E1701525	50.23	24.23
	E1800455	49.97	24.98
	M0200454	55.49	11.46
	M0302928	51.58	1.06
	M0307656	49.3	33.34
	M1400154	60.66	2.93
	M1501367	62.34	0.14
	M1700532	38.88	6.88
	M2101650	64.77	7.7
	M2200263	41.57	43.1
<i>Ismenius Lacus</i>	M2301291	48	24.55
	M2301932	57.41	6.71
	E2101593	61.79	338.38
	E2201104	46.56	335.24
	E2201598	46.65	302.8
	M0201627	51.96	300.6

	M1501423	46.3	311.31
	R0100562	45.68	331.98
	R0200497	61.37	336.11
	E2101593	61.79	338.38
	E2101207	61.89	338.25
	R0200497	61.37	336.11
	E2101141	53.84	323.84
	E2001518	61.33	317.07
	E2201104	46.56	335.24
	R0100562	45.68	331.98
	E2201598	46.65	302.8
<i>Casius</i>	E2200059	62	289.55
	R0100902	59	277.91
	E1900461	45.35	271.71
	E2301288	42.31	273.92
	E2301388	43.62	270.09
	R0100604	47.19	258.7
	E2300331	45.69	257.76
	E2001390	45.73	260.19
	R0200414	45.34	262.86
	R0201210	45.38	263.05
	R0200014	41.31	262.03
	E2300337	42.26	285.8
	R0201337	43.51	287.03
	M0400859	40.83	280.77
	SP124904	40.84	274.03
	SP239703	40.97	269.76
	M0400988	41.24	264.35
	M0304531	41.76	284.4
	M0306811	41.86	257.82
	M0404181	41.93	274.87
	SP248805	41.94	273.87
	M0100973	42.16	268.77
	AB103401	42.2	272.68
	M0403810	42.56	279.32
	M0402884	43.03	259.42
	SP248804	43.09	273.64
	M0202863	43.5	269.3
	M0100582	43.69	273.28
	M0400861	43.86	281.3
	M0402704	44.09	276.14
	M0401631	44.33	272.68
	M0304331	44.46	272.8
	M0301533	44.48	258.52
	M0100379	44.49	261.22
	M0104558	44.5	276.11
	M0400022	44.77	261.55
	M0303023	45.02	286.16
	M0104325	45.2	264.03
	M0401834	45.32	285.04



---

M0402077	45.52	268.56
M0000215	45.65	259.84
M0400990	45.75	265.15
M0401440	45.77	260.79
M0403662	45.8	267.75
M0203335	46.19	265.39
M0305064	46.27	264.24
FHA00447	46.4	269.96
M0103868	46.6	268.55
M0304830	47.06	268.83
M0302113	47.41	266.79
M0400453	47.46	286.31
FHA01060	47.62	265.47
M0404325	47.7	288.07
FHA01129	47.7	277.74
M0202032	47.96	266.76
M0203874	48.82	261.5
M0304092	48.83	261.46
M0303674	49.45	294.68
M0001625	50.04	260.14
M0201433	50.47	259.53
M0203876	53.62	262.54
FHA00857	53.66	258.77
M0202833	60.8	244.46
M0401632	61.02	276.48
M0401037	63.76	298.21
M0401037	63.76	298.21
M0303676	64.05	298.47
M1301380	44.81	259.27
M1501497	46.05	266.11
M1501927	46.25	281.6
M1301382	48.92	260.07
M2202520	40.46	276.35
M2101302	41.96	272.56
M1901929	43.71	267.16
M2301412	44.35	294.07
M1901326	44.35	272.11
M1901721	45.14	259.46
M2300078	45.35	260.85
M1901481	46.03	268.12
M2001414	46.17	257.88
M2301857	46.47	266.2
M2201583	47.65	285.68
M2201173	49.07	265.44
M1900956	54.58	254.02
M1900234	66.16	278.81
E0301748	38.83	286.54
E0502102	40.91	276.95
E0500488	41.68	277.23
E0401564	41.77	277.42

---

---

	E0500784	42.07	286.22
	E0302633	42.37	285.01
	E0100408	42.6	262.14
	E0501956	42.67	264.71
	E0402467	43.27	259.63
	E0401425	43.57	265.19
	E0201703	43.63	272.26
	E0500637	44.05	261.5
	E0503354	44.32	279.24
	E0100542	44.53	258.54
	E0302404	44.72	260.4
	E0200880	44.93	274.91
	E0502243	45.14	267.55
	E0400442	45.54	267.46
	E0502576	45.84	258.07
	E0201397	46.03	268.07
	E0401735	46.4	274.65
	E0502246	51.29	262.77
	E0302635	61.98	289.48
	E0502424	63.74	278.63
	E0202108	64.01	269.75
	E0500113	64.54	289.86
	E0300299	64.68	292.92
	E1202545	40.33	270.56
	E1202313	41.09	274.56
	E1004747	41.65	272.54
	E1203233	42.4	287.96
	E1100873	44.59	261.54
	E1102077	45.06	278.78
	E1202984	45.24	263.68
	E1301059	38.7	260.2
	E1700431	42.2	287.61
	E1600270	42.92	264.67
	E1300967	44.21	277.27
	E1700959	45.43	272.37
	E1601195	45.78	298.98
	E1600139	46.67	269.27
	E1701205	50.29	265.39
<i>Cebrenia</i>	E1200641	38.33	186.46
	E1601104	61.08	204.14
	E1700838	54.67	220.89
	M0200280	63.75	218.53
	M0201401	63.49	234.17
	M0302586	60.8	236.79
	M0306039	37.94	180.12
	M1500996	38.79	208.62
	M1501410	47.86	225.67
	M1800373	54.75	220.91
	M1801383	50.29	185.47
	M2000146	45.56	185.29

---

M2000683	60.7	212.64
M2100490	60.56	186.84
M2201098	63.9	199.58
M2202499	60.3	194.55
M2300419	59.97	239.67
M2301399	41.48	236.23

### Appendix 3

Table A2. Appearance of MOC images: sublimation, icy, or intermediate

Quadrangle	MOC image number	Latitude (degrees North)	Longitude (degrees West)	Appearance
<i>Diacria</i>	M1501063	39.46	163.6	intermediate
	E1202507	42.69	156.32	intermediate
	M1801140	42.85	164.06	intermediate
	FHA00694	45.62	175.4	intermediate
	M2200677	62.7	121.6	intermediate
	M0001948	40.16	139.54	sublimation
<i>Arcadia</i>	M0200976	59.03	94.22	icy
	M2101277	61.28	105.09	icy
	M1900018	61.41	97.54	icy
	M2000948	62.12	90.34	icy
	E1501561	62.45	80.42	icy
	M0200978	63.39	95.55	icy
	E0400073	64.64	114.82	icy
	E0301639	65.04	108.1	icy
	E0502689	51.72	71.17	intermediate
	E1101784	56.77	97.03	intermediate
	M2000659	56.86	97.24	intermediate
	E0100508	58.07	89.67	intermediate
	M2301007	60.85	109.38	intermediate
	M0204284	60.93	71.73	intermediate
	M2201038	54.27	82.5	sublimation
	M0200454	55.49	11.46	icy
	M2301932	57.41	6.71	icy
	M1400154	60.66	2.93	icy
<i>Mare Acidalium</i>	M1501367	62.34	0.14	icy
	M2101650	64.77	7.7	icy
	M1700532	38.88	6.88	intermediate
	E1700211	47.12	34.57	intermediate
	M0307656	49.3	33.34	intermediate
	E1700671	49.95	23.26	intermediate
	E1800455	49.97	24.98	intermediate
	E0501785	50.08	24.22	intermediate
	E0300154	50.84	18.62	intermediate
	E0300457	60.7	58.68	intermediate
	M2200263	41.57	43.1	sublimation
	M2301291	48	24.55	sublimation
	E1300642	51.54	12.41	sublimation

<i>Ismenius Lacus</i>	M0302928	51.58	1.06	sublimation
	E2001518	61.33	317.07	both
	R0200497	61.37	336.11	both
	R0200497	61.37	336.11	icy
	E2101593	61.79	338.38	icy
	E2101593	61.79	338.38	icy
	E2101207	61.89	338.25	icy
	R0100562	45.68	331.98	intermediate
	M1501423	46.3	311.31	intermediate
	M0201627	51.96	300.6	intermediate
	E2101141	53.84	323.84	intermediate
	R0100562	45.68	331.98	sublimation
	E2201104	46.56	335.24	sublimation
	E2201104	46.56	335.24	sublimation
	E2201598	46.65	302.8	sublimation
	E2201598	46.65	302.8	sublimation
<i>Casius</i>	E0502246	51.29	262.77	ice
	E0302635	61.98	289.48	ice
	E0502424	63.74	278.63	ice
	M0401037	63.76	298.21	ice
	E0202108	64.01	269.75	ice
	M0303676	64.05	298.47	ice
	E0500113	64.54	289.86	ice
	E0300299	64.68	292.92	ice
	M1900234	66.16	278.81	ice
	R0100902	59	277.91	icy
	E2200059	62	289.55	icy
	E1301059	38.7	260.2	intermediate
	E0301748	38.83	286.54	intermediate
	M0400859	40.83	280.77	intermediate
	M0304531	41.76	284.4	intermediate
	M2101302	41.96	272.56	intermediate
	E0500784	42.07	286.22	intermediate
	E0302633	42.37	285.01	intermediate
	M0403810	42.56	279.32	intermediate
	E1600270	42.92	264.67	intermediate
	M0400861	43.86	281.3	intermediate
	M0100379	44.49	261.22	intermediate
	E0200880	44.93	274.91	intermediate
	M1901721	45.14	259.46	intermediate
	E0400442	45.54	267.46	intermediate
	M2001414	46.17	257.88	intermediate
	M0400453	47.46	286.31	intermediate
	M2201583	47.65	285.68	intermediate
	M0404325	47.7	288.07	intermediate
	FHA01129	47.7	277.74	intermediate
	M1301382	48.92	260.07	intermediate
	M0303674	49.45	294.68	intermediate
	M0203876	53.62	262.54	intermediate
	M0202833	60.8	244.46	intermediate

---

M0401632	61.02	276.48	intermediate
M0401037	63.76	298.21	intermediate
E1202545	40.33	270.56	sublimation
M2202520	40.46	276.35	sublimation
SP124904	40.84	274.03	sublimation
E0502102	40.91	276.95	sublimation
SP239703	40.97	269.76	sublimation
E1202313	41.09	274.56	sublimation
M0400988	41.24	264.35	sublimation
R0200014	41.31	262.03	sublimation
E1004747	41.65	272.54	sublimation
E0500488	41.68	277.23	sublimation
E0401564	41.77	277.42	sublimation
M0306811	41.86	257.82	sublimation
M0404181	41.93	274.87	sublimation
SP248805	41.94	273.87	sublimation
M0100973	42.16	268.77	sublimation
AB103401	42.2	272.68	sublimation
E2300337	42.26	285.8	sublimation
E2301288	42.31	273.92	sublimation
E1203233	42.4	287.96	sublimation
E0501956	42.67	264.71	sublimation
SP248804	43.09	273.64	sublimation
E0402467	43.27	259.63	sublimation
M0202863	43.5	269.3	sublimation
R0201337	43.51	287.03	sublimation
E0401425	43.57	265.19	sublimation
E0201703	43.63	272.26	sublimation
M0100582	43.69	273.28	sublimation
M1901929	43.71	267.16	sublimation
E0500637	44.05	261.5	sublimation
M0402704	44.09	276.14	sublimation
E0503354	44.32	279.24	sublimation
M0401631	44.33	272.68	sublimation
M2301412	44.35	294.07	sublimation
M1901326	44.35	272.11	sublimation
M0304331	44.46	272.8	sublimation
M0301533	44.48	258.52	sublimation
M0104558	44.5	276.11	sublimation
E0100542	44.53	258.54	sublimation
E0302404	44.72	260.4	sublimation
M0400022	44.77	261.55	sublimation
M1301380	44.81	259.27	sublimation
M0303023	45.02	286.16	sublimation
E0502243	45.14	267.55	sublimation
M0104325	45.2	264.03	sublimation
E1202984	45.24	263.68	sublimation
M0401834	45.32	285.04	sublimation
R0200414	45.34	262.86	sublimation
M2300078	45.35	260.85	sublimation

---

	E1900461	45.35	271.71	sublimation
	R0201210	45.38	263.05	sublimation
	E1700959	45.43	272.37	sublimation
	M0402077	45.52	268.56	sublimation
	M0000215	45.65	259.84	sublimation
	E2300331	45.69	257.76	sublimation
	E2001390	45.73	260.19	sublimation
	M0400990	45.75	265.15	sublimation
	M0401440	45.77	260.79	sublimation
	E1601195	45.78	298.98	sublimation
	M0403662	45.8	267.75	sublimation
	E0502576	45.84	258.07	sublimation
	M1901481	46.03	268.12	sublimation
	E0201397	46.03	268.07	sublimation
	M1501497	46.05	266.11	sublimation
	M0203335	46.19	265.39	sublimation
	M1501927	46.25	281.6	sublimation
	M0305064	46.27	264.24	sublimation
	FHA00447	46.4	269.96	sublimation
	E0401735	46.4	274.65	sublimation
	M2301857	46.47	266.2	sublimation
	M0304830	47.06	268.83	sublimation
	M0302113	47.41	266.79	sublimation
	FHA01060	47.62	265.47	sublimation
	M0202032	47.96	266.76	sublimation
	M0203874	48.82	261.5	sublimation
	M0304092	48.83	261.46	sublimation
	M2201173	49.07	265.44	sublimation
	M0001625	50.04	260.14	sublimation
	E1701205	50.29	265.39	sublimation
	M0201433	50.47	259.53	sublimation
	FHA00857	53.66	258.77	sublimation
	E2301388	43.62	270.09	sublimation
	R0100604	47.19	258.7	sublimation
<i>Cebrenia</i>	M2301399	41.48	236.23	icy
	M1801383	50.29	185.47	icy
	M2202499	60.3	194.55	icy
	M2100490	60.56	186.84	icy
	M2000683	60.7	212.64	icy
	M0302586	60.8	236.79	icy
	E1601104	61.08	204.14	icy
	M0201401	63.49	234.17	icy
	M0200280	63.75	218.53	icy
	M2201098	63.9	199.58	icy
	M0306039	37.94	180.12	intermediate
	E1200641	38.33	186.46	intermediate
	M1500996	38.79	208.62	intermediate
	M2000146	45.56	185.29	intermediate
	M1501410	47.86	225.67	intermediate
	E1700838	54.67	220.89	intermediate

M1800373	54.75	220.91	intermediate
M2300419	59.97	239.67	intermediate

#### Appendix 4

Table 3A. Orientation of polygonal terrain

MOC image number	Longitude (degrees West)	Latitude (degrees North)	Orientation angle (degrees north of East)
E0401564	277.42	41.77	-4.09
E0500488	277.23	41.68	177
E0502102	276.95	40.91	180
E1102077	278.78	45.06	180
E1202313	274.56	41.09	180
M0202863	269.3	43.5	-4.12
M0303023	286.16	45.02	177
M0304331	272.8	44.46	-4.21
M0401631	272.68	44.33	176
M0402704	276.14	44.09	-4.21
M1900234	278.81	66.16	-7.33
M1901929	267.16	43.71	-4.24
M2300078	260.85	45.35	-4.29
M0401834	285.04	45.32	180
M2201583	285.68	47.65	-4.56
M0305064	264.24	46.27	-4.3
E0502243	267.55	45.14	-4.27
M0000215	259.84	45.65	-4.27
M0403810	279.32	42.56	180
M0104558	276.11	44.5	-4.21
E0200880	274.91	44.93	-4.28
M0100582	273.28	43.69	-4.17